Geophysical Journal International

Geophys. J. Int. (2019) **217,** 1179–1199
Advance Access publication 2019 February 4
GJI Geomagnetism, rock magnetism and paleomagnetism

doi: 10.1093/gji/ggy519

Preferred locations of weak surface field in numerical dynamos with heterogeneous core–mantle boundary heat flux: consequences for the South Atlantic Anomaly

Filipe Terra-Nova [1,2] Hagay Amit[2] and Gaël Choblet [2]

[1] *Departamento de Geofísica, Instituto de Astronomia, Geofísica e Ciências Atmosféricas, Universidade de São Paulo, Rua do Matão,* 1226, *Cidade Universitária,* 05508-090 *São Paulo, Brasil. E-mail: filipeterranova@iag.usp.br*
[2] *CNRS, Université de Nantes, Nantes Atlantiques Universités, UMR CNRS* 6112, *Laboratoire de Planétologie et de Géodynamique,* 2 *rue de la Houssinière, F-*44000 *Nantes, France*

Accepted 2019 February 2. Received 2018 December 4; in original form 2018 June 05

SUMMARY

The present-day geomagnetic field is characterized by a region of weak surface intensity, the so-called South Atlantic Anomaly (SAA). We identify the locations of surface intensity minima in modern, historical and archeomagnetic field models. We then investigate whether lower mantle thermal heterogeneity may explain the location of the SAA. We run numerical dynamos with heterogeneous core–mantle boundary (CMB) heat flux inferred from a lowermost mantle tomography model, varying dynamo internal control parameters as well as the amplitude of the CMB heat flux heterogeneity. Histograms of the longitude and latitude of surface intensity minima show the persistence of different locations. We find two preferred longitudes of surface intensity minima, one close to the present SAA minimum longitude. In contrast, in the dynamo models and in the archeomagnetic field models the surface intensity minima are often close to the equator, whereas the present-day SAA is at mid-latitudes. We demonstrate that the determining ingredients in dynamo models to reproduce the SAA latitude are related to north–south asymmetries of reversed and normal geomagnetic flux on the CMB. The imposed heterogeneous heat flux leads to more convective and magnetic activities in the Northern Hemisphere. Large time-average upwelling structure below the South Atlantic in the dynamo models correlates well with the present-day SAA region. Scaling laws analysis indicates that the persistence of surface minima longitudes is favored by slow rotation, strong convection and large heat flux heterogeneity. Furthermore, increasing mantle control yields two preferred longitudes and southern surface minima, the latter indicating that the present-day southern location of the SAA is mantle controlled. However, the rareness of mid-latitude minima in dynamo models and archeomagnetic field models leads us to speculate that the SAA mid-latitude value at present is possibly unusual.

Key words: Heat flow; Archaeomagnetism; Dynamo: theories and simulations; Magnetic field variations through time.

1 INTRODUCTION

The outer core of the Earth is composed of an electrically conductive liquid. The dynamics of this fluid are governed not only internally but also by a set of boundary conditions, for example a thermal constraint describing the heat flux across the core–mantle boundary (CMB). Previous studies showed that numerical dynamos with imposed laterally heterogeneous CMB heat flux inferred from seismic shear wave velocity anomalies can explain various persistent morphological features of the present-day geomagnetic field, most notably the locations of intense flux patches (Olson & Christensen 2002; Gubbins *et al.* 2007; Aubert *et al.* 2008; Davies *et al.* 2008). Fig. 1 illustrates how thermal heterogeneity in the lowermost mantle may affect core dynamics (as previously described by e.g. Gubbins 2003): A colder region of the lowermost mantle corresponds to a larger CMB heat flux, colder outer core fluid and downwelling which concentrates magnetic flux, yielding a stronger local field. Conversely, a hotter region of the lowermost mantle corresponds to core fluid upwelling and a weaker (or reversed) local field (Terra-Nova *et al.* 2016).

Since the advent of intensity measurements, it has been observed that reversed geomagnetic flux regions on the CMB have been expanding and intensifying in time together with the decreasing geomagnetic axial dipole (e.g. Gubbins 1987; Jackson *et al.*

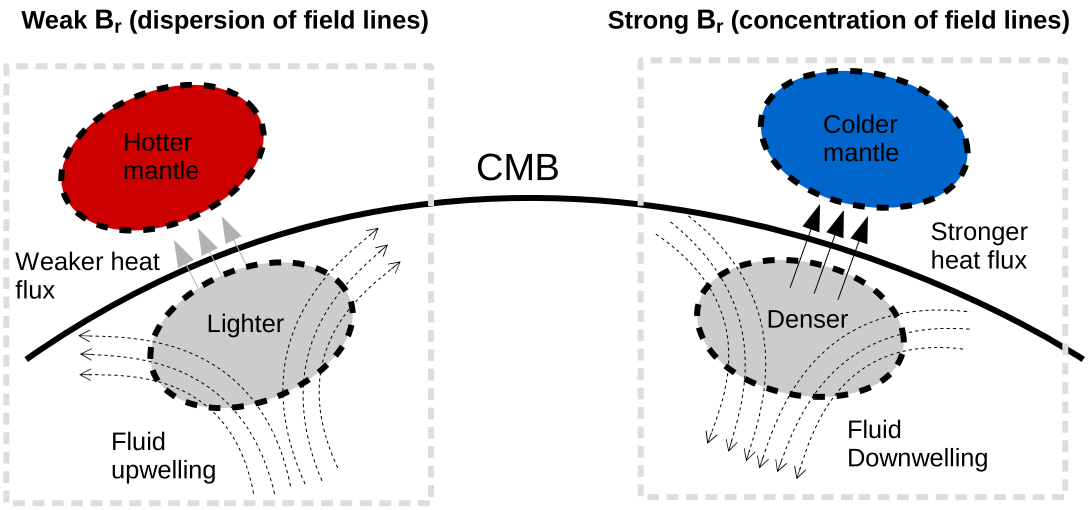

Figure 1. Schematic illustration of concentration and dispersion of magnetic poloidal field lines on the CMB due to lowermost mantle thermal heterogeneity.

2000; Hulot *et al.* 2002; Olson & Amit 2006; Finlay 2008; Finlay *et al.* 2016; Metman *et al.* 2018). Metman *et al.* (2018) showed that the historical decrease of the geomagnetic dipole intensity is linked to the time-dependence of the area of reversed flux on the CMB. At Earth's surface, a region of weak magnetic field intensity, the so-called South Atlantic Anomaly (SAA), is observed (e.g. Olson & Amit 2006; Hartmann & Pacca 2009). The SAA is related to prominent geomagnetic flux patches on the CMB (Terra-Nova *et al.* 2017), which may be mantle-controlled (Gubbins 2003; Terra-Nova *et al.* 2016), hence the SAA may also be mantle controlled.

There are arguments for and against feasibly detectable mantle control on the SAA. Based on data assimilation, Aubert (2015) predicted westward drift of the SAA until 2115, when the anomaly would reach the West Pacific. In contrast, some archeomagnetic field models contain recurrence of reversed flux on the CMB and minimum surface intensity both in the South Atlantic (Brown *et al.* 2018; Hellio & Gillet 2018). In addition, based on archeological materials from Africa and South America, it was argued that rapid local temporal geomagnetic field variations in these regions are attributed to the SAA time evolution (e.g. Hartmann *et al.* 2010, 2011; Tarduno *et al.* 2015; Poletti *et al.* 2016; Shah *et al.* 2016; Hare *et al.* 2018; Trindade *et al.* 2018). Accordingly, the SAA may be locked to the South Atlantic at the surface, perhaps alternating between Africa and South America. However, it is worth noting that the validity of inferring global surface intensity minima from local intensity time-series has not yet been demonstrated. If indeed the SAA is persistent, its location may be related to lowermost mantle heterogeneity (Gubbins 2003; Tarduno *et al.* 2015).

Intense high-latitude magnetic flux patches in the time-average field of dynamo models with a Y_2^2 outer boundary heat flux pattern were found to be azimuthally shifted with respect to the longitudes of positive heat flux anomalies (Olson & Christensen 2002; Aubert *et al.* 2007; Takahashi *et al.* 2008), where the amount of shift depends on the dynamo control parameters. However, in numerical dynamos with tomographic heat flux neither the existence of such a shift nor its dependence on the dynamo parameters were systematically studied. Moreover, the relation between surface intensity minima and CMB heat flux using tomographic dynamo models has not been explored. This relation introduces an additional complexity because the relation between the radial field at the CMB and the intensity at the surface is non-linear (Gubbins & Roberts 1983; Johnson & Constable 1997; Constable 2007; Terra-Nova *et al.* 2017).

In this paper, we introduce procedures to analyse the locations of surface minima in both geomagnetic field models and numerical dynamo models with heterogeneous outer boundary heat flux inferred from lowermost mantle seismic tomography. We compare between the observed and modelled surface minima to determine whether the present-day location of the SAA is a persistent feature of the geodynamo controlled by the mantle heterogeneity. In addition we examine the time dependence of the surface field minima and its relation to core fluid flow and CMB heat flux while systematically changing the dynamo control parameters.

In Section 2, we describe the dynamo models, the identification method of surface intensity minima and the estimation of magnetic flux asymmetries. Section 3 presents the results of surface intensity minima identification in geomagnetic field models and numerical dynamos with special attention to their latitude discrepancy. In this section, we also relate north–south asymmetries of reversed and normal flux to the latitude of the surface intensity minima. Finally, in Section 4 we discuss some possible geophysical implications, in particular the detectability of mantle control on the locations of surface intensity minima and the prospect that the SAA is persistent.

2 METHODS

2.1 Numerical dynamos

Numerical dynamo simulations provide self-consistent solutions to the full set of magnetohydrodynamic (MHD) equations, describing conservation of momentum, electromagnetic induction, conservation of heat (or co-density), incompressibility and non-existent magnetic monopole. These equations can be expressed in non-dimensional form (e.g. Wicht 2002) as, respectively:

$$E\left(\frac{\partial \mathbf{u}}{\partial t}+\mathbf{u}\cdot\nabla\mathbf{u}-\nabla^2\mathbf{u}\right)+2\hat{z}\times\mathbf{u}+\nabla P = Ra\frac{\mathbf{r}}{r_o}C+\frac{1}{Pm}(\nabla\times\mathbf{B})\times\mathbf{B}, \quad (1)$$

$$\frac{\partial \mathbf{B}}{\partial t}=\nabla\times(\mathbf{u}\times\mathbf{B})+\frac{1}{Pm}\nabla^2\mathbf{B}, \quad (2)$$

$$\frac{\partial C}{\partial t} + \mathbf{u}\cdot\nabla C = \frac{1}{Pr}\nabla^2 C + \epsilon, \tag{3}$$

$$\nabla\cdot\mathbf{u} = 0, \tag{4}$$

$$\nabla\cdot\mathbf{B} = 0, \tag{5}$$

where $\mathbf{u}$ is the fluid velocity, $\hat{z}$ the direction of the axis of rotation, P the pressure, $\mathbf{r}$ the radial position vector, r_o the core radius, C the co-density, $\mathbf{B}$ the magnetic field and ε the buoyancy source or sink. The co-density is given by $C = \alpha T + \beta\xi$ where T is temperature, ξ is light elements concentration, and α and β are their respective expansivities. Eqs (1)–(3) are governed by four (internal) control parameters. The Ekman number represents the ratio of viscous to Coriolis forces:

$$E = \frac{\nu}{\Omega D^2}. \tag{6}$$

The heat flux based Rayleigh number represents the convection vigor versus retarding forces:

$$Ra = \frac{\alpha g_0 q_0 D^4}{\kappa\nu k}. \tag{7}$$

The Prandtl number and the magnetic Prandtl number are ratios of diffusivities:

$$Pr = \frac{\nu}{\kappa}, \tag{8}$$

$$Pm = \frac{\nu}{\eta}. \tag{9}$$

In (6)–(9) Ω is the rotation rate, ν the kinematic viscosity, D the shell thickness, g_0 the gravitational acceleration at the outer boundary, q_0 the mean outer boundary heat flux, k the thermal conductivity, κ the thermal diffusivity and η the magnetic diffusivity. In the following, we explored control parameters (Table 1) that produce dynamos with non-reversing dipole dominated fields (e.g. Kutzner & Christensen 2002) which roughly resemble Earth's field morphology during a chron.

All dynamo simulations were carried out with rigid and electrically insulating conditions at both boundaries. The spherical shell has an inner to outer core radii ratio of 0.35, corresponding to the present-day Earth's core geometry. We impose on the outer boundary of most of the simulations a heat flux pattern (Fig. 2) based on a tomographic model of seismic shear wave velocity anomalies at the lowermost mantle (Masters *et al.* 2000). The amplitude of the imposed heat flux heterogeneity is quantified by (Olson & Christensen 2002)

$$q^* = \frac{q_{max} - q_{min}}{2q_0}, \tag{10}$$

where q_{max} and q_{min} are the maximum and minimum heat flux, respectively. Here q^* is an additional (boundary) control parameter to be explored. For the inner boundary fixed codensity is imposed (e.g. Aubert *et al.* 2008; Olson *et al.* 2017). Additional simulations were run with a homogeneous heat flux as references cases. In these models, no preferred longitude of local surface intensity minimum is expected if the simulation time is long enough. All dynamo simulations were run for more than two diffusion times (except for case 28 where the computational cost was high). Typical time between analysed snapshots ranges ≈0.10–0.68 advection times. The number of Chebyshev radial grid points ranges $N_r = 41 - 97$ and in the tangential direction the solutions are expanded up to spherical harmonic degree $n_{max} = 64 - 106$ (Table 1).

Mantle control in numerical dynamos has been commonly explored by time-average properties (e.g. Olson & Christensen 2002; Aubert *et al.* 2008). While time-averaging allows access to robust features, it might miss some aspects of the solution. For example, drifting features might be averaged out. Detailed analysis of long and dense time-series of snapshots provides a more complete description of the models (e.g. Amit *et al.* 2010). We therefore analyse long time-series of the field in order to explore mantle control on field intensity minima.

For each dynamo model we report several output parameters (Table 1). Two main conventional output parameters were monitored. The magnetic Reynolds number $Rm = Pm\sqrt{2E_{kin}}$ is based on the time-average kinetic energy in the shell E_{kin}. The relative dipole field strength on the outer boundary (Christensen & Aubert 2006) is

$$f_{dip} = \sqrt{\frac{\left(\frac{r_a}{r_0}\right)^6 \frac{4}{3}\left((g_1^0)^2 + (g_1^1)^2 + (h_1^1)^2\right)}{\left(\frac{r_a}{r_0}\right)^{2n+4} \sum_{n=1}^{12}\sum_{m=0}^{n} \frac{(n+1)^2}{(2n+1)}\left((g_n^m)^2 + (h_n^m)^2\right)}}, \tag{11}$$

where n and m are spherical harmonic degree and order respectively, g_n^m and h_n^m are the field's internal Gauss coefficients and r_a the mean radius of Earth's surface. In addition we characterize the persistent locations of local minima of surface intensity as described below.

2.2 Identification of surface intensity minima

We separate the analysis into histograms of longitude and latitude due to the distinctive processes that may determine each coordinate. Neither the MHD equations nor the core geometry contain any preferred longitude. Therefore, statistically preferred longitudes of geomagnetic flux features on the CMB are inevitably controlled by boundary heterogeneity (e.g. Olson & Christensen 2002). Indeed it was found that the longitudinal dependence of latitude integrated magnetic flux (of normal or reversed polarity) and latitude integrated lower mantle seismic anomalies (positive or negative) are correlated (Gubbins 2003; Terra-Nova *et al.* 2016). In contrast, special latitudes appear both in the MHD equations and in the core geometry. The Coriolis force yields pole-to-equator differences in thermal wind morphology (e.g. Amit *et al.* 2008) because at the poles gravity is parallel to the rotation axis whereas at the equator gravity is perpendicular to the rotation axis. In addition, the presence of the inner core leads to a flow barrier at the tangent cylinder (Aurnou *et al.* 2003). Consequently, intense normal flux patches are concentrated at the latitude where the tangent cylinder intersects the CMB (e.g. Olson *et al.* 1999). Even when the CMB heat flux is concentrated at low latitudes the tangent cylinder effect may persist (Amit & Choblet 2012; Amit *et al.* 2015b). The difference between processes determining longitude and latitude of magnetic flux patches is evident when a spherical harmonic Y_2^2 CMB heat flux pattern is imposed. Two intense flux patches appear at each hemisphere demonstrating that the order 2 is well recorded in longitude, but the patches appear at the tangent cylinder latitude and not at the equator where the CMB heat flux is largest (e.g. Olson & Christensen 2002; Aubert *et al.* 2007).

The following analysis was applied to both geomagnetic field models and output from numerical dynamos. At each time step t_i

Table 1. Dynamo models setup and results.

Case	E	Ra	Pm	q^*	N_r	n_{max}	Rm	f_{dip}	$\mathcal{P}_\phi$	$\mathcal{P}_\lambda$	h_W	N_F	σ_{N_F}
1	3×10^{-4}	3×10^{6}	4	0	41	64	368	0.58	None	−0.2	2.46×10^{-3}	2.70	0.73
2	3×10^{-4}	5×10^{5}	4	0.7	41	64	107	0.66	None	−0.3	3.75×10^{-3}	2.20	0.69
3	3×10^{-4}	1×10^{6}	4	0.7	41	64	166	0.57	−79.3, 78.2	−0.8	5.61×10^{-3}	2.23	0.66
4	3×10^{-4}	1×10^{6}	4	1.0	41	64	168	0.54	−91.4	−0.1	6.58×10^{-3}	2.34	0.67
5	3×10^{-4}	1×10^{6}	9	0.7	41	64	356	0.50	−76.5	0.4	4.53×10^{-3}	2.30	0.70
6	3×10^{-4}	3×10^{6}	3	0.7	41	64	236	0.56	−65.52, 103.4	−1.0	7.42×10^{-3}	2.47	0.67
7	3×10^{-4}	3×10^{6}	4	0.7	41	64	312	0.51	−61.5, 105.1	−1.7	7.35×10^{-3}	2.56	0.72
8	3×10^{-4}	3×10^{6}	4	1.0	41	64	314	0.49	−63.8, 96.8	−3.2	9.26×10^{-3}	2.49	0.69
9	3×10^{-4}	3×10^{6}	9	0.4	41	64	248	0.48	−80.2, 56.6	−1.7	5.19×10^{-3}	2.77	0.84
10	3×10^{-4}	3×10^{6}	9	0.7	41	64	662	0.42	−53.6, 99.5	−0.9	6.06×10^{-3}	2.63	0.77
11	3×10^{-4}	3×10^{6}	9	1.0	41	64	677	0.39	−57.0, 86.2	−3.0	6.71×10^{-3}	2.62	0.81
12	3×10^{-4}	5×10^{6}	4	0.4	41	64	419	0.47	−47.7, 136.9	−2.8	5.57×10^{-3}	2.54	0.78
13	3×10^{-4}	5×10^{6}	4	0.7	41	64	428	0.43	−49.5, 125.1	−5.7	7.57×10^{-3}	2.70	0.84
14	1×10^{-4}	3×10^{7}	2	0	49	64	328	0.70	None	0.1	2.14×10^{-3}	2.63	0.78
15	1×10^{-4}	3×10^{6}	3	0.7	49	64	136	0.68	None	0.0	3.19×10^{-3}	2.21	0.68
16	1×10^{-4}	3×10^{6}	4	0.7	49	64	178	0.61	None	0.6	2.96×10^{-3}	1.90	0.76
17	1×10^{-4}	5×10^{6}	4	0.7	49	64	238	0.57	None	0.2	3.01×10^{-3}	2.14	0.75
18	1×10^{-4}	1×10^{7}	4	0.7	49	64	350	0.55	None	0.0	3.80×10^{-3}	2.35	0.71
19	1×10^{-4}	3×10^{7}	2	0.4	65	96	331	0.69	101.8	−0.2	4.44×10^{-3}	2.58	0.71
20	1×10^{-4}	3×10^{7}	2	0.7	49	64	332	0.66	−53.2, 108.4	−0.6	5.39×10^{-3}	2.49	0.74
21	1×10^{-4}	3×10^{7}	2	1.0	65	96	332	0.62	−56.7,102.6	−1.9	7.36×10^{-3}	2.51	0.70
22	1×10^{-4}	4×10^{7}	2	0.7	65	96	398	0.65	−43.4,117.3	−2.3	8.37×10^{-3}	2.43	0.68
23	1×10^{-4}	4×10^{7}	2	1.0	65	96	405	0.60	−54.6,118.4	−3.6	7.38×10^{-3}	2.59	0.71
24	3×10^{-5}	4×10^{7}	0.8	0	65	96	95	0.87	None	0.2	1.71×10^{-3}	2.46	0.79
25	3×10^{-5}	4×10^{7}	0.8	0.4	65	96	100	0.82	None	0.5	3.65×10^{-3}	2.28	0.83
26	3×10^{-5}	8×10^{7}	0.8	0.7	81	106	130	0.80	None	0.3	2.54×10^{-3}	2.29	0.76
27	3×10^{-5}	8×10^{7}	0.8	1.0	81	106	131	0.79	None	−0.1	2.63×10^{-3}	2.32	0.70
28	3×10^{-5}	9×10^{7}	2	1.0	97	106	332	0.64	113.2	1.1	3.78×10^{-3}	2.15	0.73

Control parameters E, Ra, Pm and q^* are defined in (6)–(10). In all models $Pr = 1$. The number of radial grid points in the shell is N_r, and n_{max} is the maximum harmonic degree. The magnetic Reynolds number is calculated from the time-average kinetic energy in the shell. The outer boundary dipolarity f_{dip} is defined in (11). $\mathcal{P}_\phi$ and $\mathcal{P}_\lambda$ are the persistent locations of local minima of surface intensity in longitude and latitude, respectively. The typical height h_W measures the persistence of surface intensity minima peaks, N_F is the mean number of local surface intensity minima per snapshot and σ_{N_F} is its standard deviation.

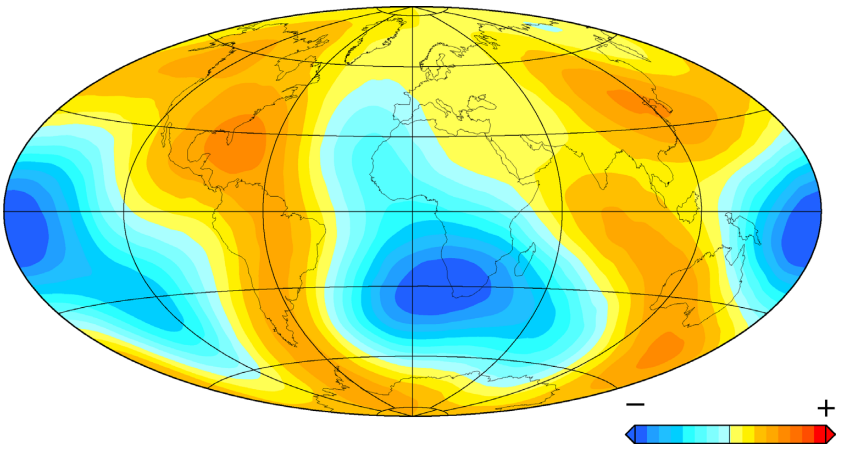

Figure 2. Heterogenous heat flux anomalies based on tomographic seismic shear wave anomalies at the lowermost mantle (Masters *et al.* 2000) truncated at spherical harmonic degree 6. This pattern was imposed as a heterogeneous outer boundary heat flux in the dynamo models. Red/blue corresponds to large/low heat flux (and thus colder/hotter mantle), respectively.

the surface field snapshots were calculated using the Gauss coefficients $g_n^m(t_i)$ and $h_n^m(t_i)$ truncated at spherical harmonic degree and order n_{max}. For all numerical dynamo field models $n_{max} = 14$ (corresponding to the highest resolution of the modern and historical core fields), while for the geomagnetic field n_{max} is model dependent (see Terra-Nova *et al.* 2016). The histograms are constructed as follows:

(i) For every snapshot, we identified the local surface intensity minima F_{min} and their longitudes ϕ_{Fmin} and latitudes λ_{Fmin}.

(ii) In order to focus on large-scale features, if in a snapshot a pair of F_{min} are separated by a great circle distance smaller than 10° (which is usually not the case but does occur seldom in some snapshots of the dynamo models), these two minima were linearly interpolated to a single minimum. We calculated the time-average number of minima per snapshot N_F and the corresponding standard deviation σ_{N_F} for each field model.

(iii) Each identified F_{min} was weighted by its relative intensity

$$W_{Fmin} = \frac{< F > - F_{min}}{< F >}, \tag{12}$$

where $<>$ denotes RMS (root mean squared) values over the spherical surface.

(iv) For each dynamo model, we constructed histograms H_ϕ and H_θ by summing the respective weights W_ϕ and W_θ in time and space over 10° bins in longitude and in latitude, respectively. Because we use uniform bin size in degrees, a geometric correction was applied to the latitude weight

$$W_\theta = W_{F_{min}} / \sin(\theta_{F_{min}}), \tag{13}$$

where θ is colatitude, while for longitude $W_\phi = W_{F_{min}}$. This geometric correction merely accounts for the smaller area enclosed by higher latitude bins. Finally, larger W_ϕ or W_θ correspond to weaker surface minimum and a more significant F_{min} in our analysis.

We then introduce quantitative diagnostics for these histograms. Since dynamo models with homogeneous outer boundary heat flux are expected to have equally distributed positions of surface minima intensity in longitude, we also calculated the typical height h_W of the integrated W_ϕ histogram peaks:

$$h_W = \sqrt{\frac{1}{N_i} \sum_i \left(H_\phi - \bar{H}_\phi\right)^2}, \tag{14}$$

where i denotes summation over multiple bins, $N_i = 36$ is the number of histogram bins, H_ϕ the histogram peak height and $\bar{H}_\phi$ its average. h_W represents the deviation of the longitude histograms peaks from a flat distribution. The larger h_W the more persistent are longitudes represented by the histograms peaks. Due to the multiple-peaks, rough longitude histograms, we smoothed these histograms by applying a moving average thus avoiding over interpretation of small-scale features related to the finite averaging time. Next we applied a cutoff (see below) to interpret only persistent peaks in the histograms. Then using second order polynomials centred at these prominent peaks (one polynomial for each peak), non-discrete preferred longitudes of F_{min} were locally interpolated. In contrast, due to the single peak latitude histograms, the last part of the scheme for latitude simply consists of a weighted average using (13):

$$P_\lambda = \frac{\sum_j (W_\theta \lambda_{Fmin})_j}{\sum_j (W_\theta)_j}, \tag{15}$$

where j denotes summation over multiple field intensity minima at all snapshots. The summation in (15) therefore corresponds to summation over the spherical CMB surface and time. These general identification schemes were validated by thorough empirical trials. The final results are the persistent locations of local minima of surface intensity in longitude and latitude $\mathcal{P}_\phi$ and $\mathcal{P}_\lambda$, respectively.

The only part of the scheme that differs between geomagnetic field models and the output from numerical dynamos is the cut-off for $\mathcal{P}_\phi$. In dynamo models, longitude histogram peaks are selected as persistent if their values exceed the mean height of its histogram peaks plus two times the typical peak height from a homogeneous dynamo model of the same Ekman number. For the geomagnetic field models such a typical height is obviously not available, because of the short period of the models as well as the presence of the heterogeneous CMB heat flux. We thus identify as persistent geomagnetic peaks those with values larger than a fraction of the global maximum, with this fraction arbitrarily chosen to be one half.

2.3 Magnetic flux hemispherical asymmetry

Deviations of surface intensity minima from equatorial locations are explained by magnetic flux hemispherical asymmetries at the CMB. For each snapshot with f_{dip} larger than a threshold value set to 0.5, we calculated the Southern Hemisphere (SH) reversed flux normalized by the reversed flux over the entire CMB by

$$S^R = \frac{\int_{SH} B_r^R \cos\theta dA}{\int_A B_r^R \cos\theta dA}, \tag{16}$$

where A is the CMB surface and B_r^R the radial field at the CMB with reversed flux:

$$B_r^R = \begin{cases} 0 & \text{, if } B_r < 0 \text{ at NH or } B_r > 0 \text{ at SH} \\ B_r & \text{, if } B_r > 0 \text{ at NH or } B_r < 0 \text{ at SH} \end{cases}. \tag{17}$$

Similarly we calculated the normalized Northern Hemisphere (NH) normal flux by

$$N^N = \frac{\int_{NH} B_r^N \cos\theta dA}{\int_A B_r^N \cos\theta dA}, \tag{18}$$

where B_r^N is the radial field at the CMB with normal flux:

$$B_r^N = \begin{cases} 0 & \text{, if } B_r > 0 \text{ at NH or } B_r < 0 \text{ at SH} \\ B_r & \text{, if } B_r < 0 \text{ at NH or } B_r > 0 \text{ at SH} \end{cases}. \tag{19}$$

In (16)–(19) the geographic equator is used to define local polarity (normal or reversed). Note that both (16) and (18) give dimensionless values between 0 and 1; in the absence of any north–south hemispherical asymmetry of magnetic flux, the two quantities are equal to 0.5.

The $\cos\theta$ factor is included in (16) and (18) because higher latitude reversed flux patches (RFPs) lead to F_{min} further from the equator whereas higher latitude normal flux patches (NFPs) provide strong local contributions to the axial dipole and lead to F_{min} closer to the equator (Terra-Nova *et al.* 2017). To illustrate these points we built two synthetic radial fields at the CMB and identified their surface intensities (Fig. 3). The synthetic fields were constructed from a background axial dipole superimposed by local patches, each modeled by a Gaussian distribution about a solid angle (Amit 2014; Terra-Nova *et al.* 2017). In synthetic field I the two hemispheres differ only by the RFPs latitudes (Fig. 3a). Here the NH RFP is at a higher latitude, $S^R < 0.5$, and indeed F_{min} is located in the NH (Fig. 3b). In synthetic field II the hemispherical asymmetry depends only on the NFPs latitudes (Fig. 3c). Here the NH NFPs are at a higher latitude, $N^N > 0.5$ and indeed F_{min} is located in the SH (Fig. 3d). Note that for these cases the intensity minima are not on the equator while without the $\cos\theta$ factor the corresponding ratios would be nevertheless equal, $S^R = N^N = 0.5$. Also note that the RFPs impact on F_{min} latitude is more pronounced than that of NFPs (Fig. 3). Defined this way, both S^R and N^N are expected to exhibit a qualitatively similar anticorrelation with the latitude of F_{min}.

If in a given snapshot $|S^R - 0.5| = |N^N - 0.5|$ (with the -0.5 terms on both sides corresponding to the excess of reversed and normal flux with respect to an equatorially symmetric configuration), one may expect the same distortion on the latitude of the surface minima by reversed and normal flux. However, different amounts of reversed and normal flux would bias the interpretation. For example, if small amounts of reversed flux appear, and only in the SH, S^R would be 1.0. However, the effect of reversed flux in this case would be negligible. In order to properly account for the hemispherical asymmetries of reversed and normal flux, we therefore considered their relative

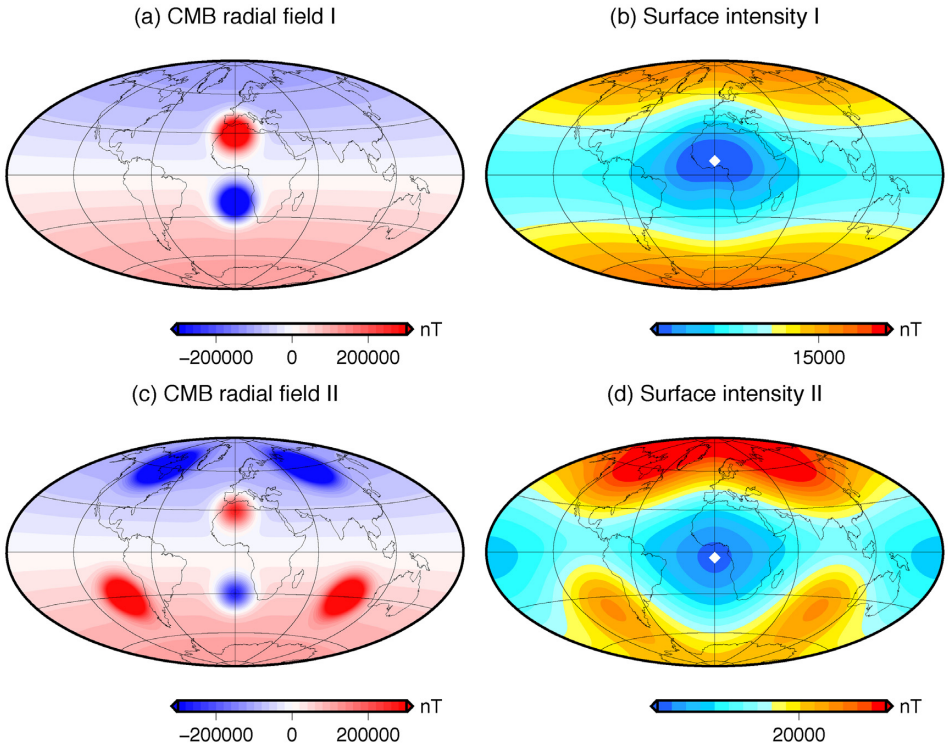

Figure 3. Synthetic radial field models at the CMB (a, c) and their corresponding surface intensities (b, d). In (a) the RFPs are at 30°N and 20°S. In (c) the NFPs are at 60°N and 30°S and the RFPs are at 30°S and 30°N. White diamonds in (b) and (d) indicate local surface intensity minima. The minima latitudes are 10°N and 4°S in (b) and (d), respectively.

magnitudes:

$$RN = \frac{\int_A B_r^R \cos\theta dA}{\int_A B_r^N \cos\theta dA}. \tag{20}$$

We used (20) to adjust (16) as follows:

$$S^{R^*} = RN(S^R - 0.5) + 0.5, \tag{21}$$

based on (21) the $|S^{R^*} - 0.5|$ and $|N^N - 0.5|$ can now be compared in terms of the contributions of reversed and normal flux hemispherical asymmetries to the latitudes of F_{min}.

Next for each snapshot we calculated the weighted average latitude of all F_{min}:

$$\lambda^*_{Fmin} = \sum_k (W_{Fmin}\lambda_{Fmin})_k, \tag{22}$$

where k denotes summation over multiple F_{min} of a given snapshot and the weight is given in (12). We searched for a linear fit to λ^*_{Fmin} versus the product of the two hemispherical asymmetries $S^{R^*}N^N$. In the absence of asymmetries $S^{R^*}N^N = 0.5^2 = 0.25$ and surface minima are expected to be on the equator. Note however that we do not constrain the linear fit to pass by the theoretically expected point (0.25,0):

$$\lambda^f_{Fmin} = aS^{R^*}N^N + b. \tag{23}$$

The linear fitting parameters a and b are determined using a conventional least squares procedure by minimizing

$$\frac{\sum_\ell \left(\sqrt{(\lambda^*_{Fmin} - \lambda^f_{Fmin})^2 d_w}\right)_\ell}{\sum_\ell (d_w)_\ell}, \tag{24}$$

where the weight d_w is the distance of each pair $(S^{R^*}N^N, \lambda^*_{Fmin})$ from the point (0.25,0) and ℓ denotes summation over all snapshots. Finally, we calculated λ^*_{Fmin} and $S^{R^*}N^N$ for all snapshots of the geomagnetic field models gufm1 and CHAOS5. It is important to emphasize that the geomagnetic field models did not participate in the fitting process which was applied only to the output of the numerical dynamos with heterogeneous outer boundary heat flux.

3 RESULTS

3.1 Surface intensity minima in geomagnetic field models

Here we present our results of the identification for local minima of surface intensity in geomagnetic field models spanning various periods. We use the modern and historical field models CHAOS5 between 1997 and 2015 (Finlay *et al.* 2015) and gufm1 between 1840 and 1990 (Jackson *et al.* 2000), respectively, both expanded until degree and order 14, the archeomagnetic field models CALS3k.3 (Korte *et al.* 2009), CALS3k.4 (Korte & Constable 2011) and pfm9k.1b (Nilsson *et al.* 2014) until degree and order 10 and A_FM-M, ASD_FM-M and ASDI_FM-M (Licht *et al.* 2013) until degree and order 5. The archeomagnetic field models span the past 3 kyr except for pfm9k.1b which covers the past 9 kyr (Table 2).

In 2015, two local minima appear, both in the South Atlantic (Fig. 4). The weakest intensity is located at inland Brazil (57°W, 26°S) (Aubert 2015; Thébault *et al.* 2015; Terra-Nova *et al.* 2017). The Africa minimum is much flatter and less intense; in earlier snapshots from CHAOS5 only the South America minimum is present.

Using the methods described above to identify persistent intensity minima we built histograms and calculated peaks of integrated W_ϕ and W_θ. In CHAOS5 one or two minima are found at a snapshot,

Table 2. Geomagnetic field models characteristics and results.

Model	Period	f_{dip}	h_W	$\mathcal{P}_\phi$	$\mathcal{P}_\lambda$	N_F	σ_{N_F}
CHAOS5	1997–2015	0.64	65.14×10^{-3}	−55.0, −5.0	−31.2	1.58	0.50
gufm1	1840–1990	0.72	20.82×10^{-3}	−41.7, 166.7	−10.5	2.16	0.47
CALS3k.4	1000BC–2000AD	0.81	7.64×10^{-3}	−55.4, 44.7, 132.8	−1.8	2.50	0.76
CALS3K.3	1000BC–2000AD	0.85	12.22×10^{-3}	−115.6, −1.8, 39.7, 46.2, 135.3	−1.1	2.31	0.84
A_FM-M	1000BC–2000AD	0.90	9.65×10^{-3}	−132.8, −67.5, −7.9, 74.3, 147.5	−2.8	2.31	0.68
ASD_FM-M	1000BC–2000AD	0.87	9.97×10^{-3}	−59.9, 52.3, 128.9	−1.2	2.35	0.64
ASDI_FM-M	1000BC–2000AD	0.89	7.81×10^{-3}	−60.3, 44.4, 131.8	−1.6	2.40	0.67
pfm9k.1b	7000BC–2000AD	0.92	10.56×10^{-3}	−74.8, 50.8, 138.7	−0.4	2.15	0.67

f_{dip} is the relative dipole strength on the outer boundary (11). The typical height h_W measures the prominence of surface intensity minima peaks. $\mathcal{P}_\phi$ and $\mathcal{P}_\lambda$ are the persistent locations of local minima of surface field intensity in longitude and latitude, respectively. N_F is the mean number of local intensity minima per snapshot and σ_{N_F} is its standard deviation.

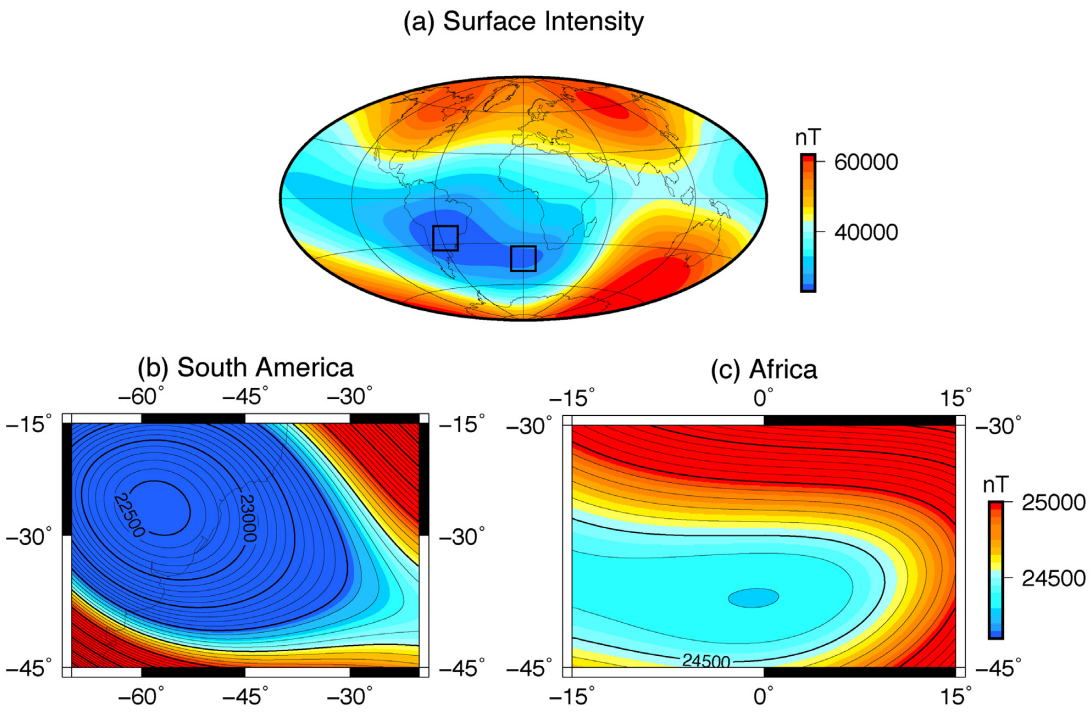

Figure 4. (a) Field intensity at Earth's surface for the CHAOS5 model (Finlay *et al.* 2015) in 2015. (b) and (c) are two zoom-ins at the regions of local intensity minima (see insets in (a)).

whereas $N_F > 2$ for the other models (see Table 2). In longitude, histograms from the modern and historical field model CHAOS5 and gufm1, respectively, exhibit two peaks of persistent locations, the archeomagnetic field models CALS3k.4, ASD_FM-M, ASDI_FM-M and pfm9k.1b have three such peaks and CALS3k.3 and A_FM-M show five peaks (Fig. 5). Both CHAOS5 and gufm1 exhibit peaks at the longitude of South America. A second less persistent peak of CHAOS5 appears at Africa. A second peak of gufm1 appears at equatorial Pacific. Overall, the peaks of all models roughly cluster in three regions: ≈60°W, ≈50°E and ≈130°E. This provides some indication that the current SAA longitude at South America is persistent, or at least one of possibly several persistent locations of local minima of surface field intensity.

In latitude, CHAOS5 exhibits two SH histogram peaks whereas gufm1 has two histogram peaks one in each hemisphere (Fig. 6). The more persistent CHAOS5 and gufm1 histogram peaks reside at mid-latitudes. In sharp contrast, the other gufm1 peak and strikingly all archeomagnetic field models persistent peaks cluster near the equator.

The preferred equatorial location of the archeomagnetic field minima is challenging to explain. It may simply be due to the lower resolution of these models compared to modern and historical field models. We tested the robustness of the surface minima equatorial location by applying a low pass filter (Terra-Nova *et al.* 2015) to a snapshot from CHAOS5:

$$\mathcal{F}(n) = \begin{cases} 1 & , \text{if } n < n_0 \\ \cos\left(\frac{\pi}{2}\left(\frac{n-n_0}{n_{max}-n_0}\right)\right) & , \text{if } n \geq n_0 \end{cases}, \tag{25}$$

where n_0 marks the beginning of the filtering and n_{max} its truncation. At $n = n_{max}$ the filter $\mathcal{F}(n_{max}) = 0$, so the highest degree considered is $n_{max} - 1$. We thus examined the sensitivity of surface minimum position and intensity to the small-scale part of the field. We explored the ranges of n_0 from 0 to 5 and n_{max} from 5 to 14. We chose degree 5 for the limits of the explored ranges because it is often considered as the limit of reliable resolution in archeomagnetic field models (e.g. Licht *et al.* 2013; Sanchez *et al.* 2016). For simplicity the filter was applied to an early snapshot of CHAOS5 (Finlay *et al.* 2015) where one minimum is found.

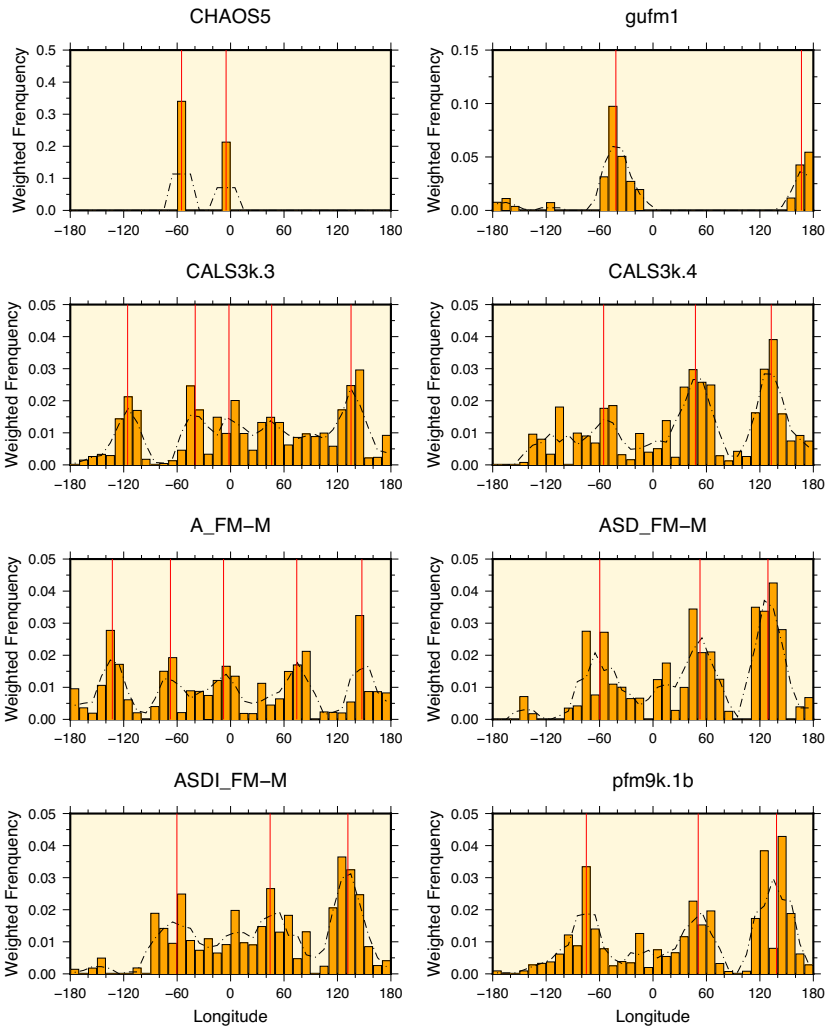

Figure 5. Histograms of local surface intensity minima in longitude. Weighted frequency is the integral over time of W_ϕ (12). The histograms are constructed with 10° bins. Red vertical lines denote persistent peaks.

Fig. 7 illustrates the effects of filtering on the radial field on the CMB (left) and on the intensity at the surface (right). The former is strongly affected by the low pass filter. As expected small-scale features progressively fade as stronger filters are applied. However, the upward continuation of the CMB potential field to the surface strongly diminishes the contribution of high degrees which are more affected by the filtering, so the surface intensity morphology is much less sensitive to the low-pass filtering. Nevertheless, it is not trivial that the specific SAA location is weakly sensitive to the filtering of the small-scales of the field (Figs 7b, d, f and h). As previously stated, the SAA location is associated with the expansion of a reversed flux region, which is associated with somewhat small-scales of the field. Note however that even with very strong filtering a signature of the reversed flux region below the South Atlantic prevails (Figs 7e and g). The strongest filtering, which corresponds to lower spatial resolution than the archeomagnetic field models, changes the minimum intensity longitude by only 6 degrees and more importantly reduces the minimum intensity latitude by 10 degrees from -26° to -16° (Fig. 7h), while a slightly less filtered field gives a reduction of only 4 degrees in the minimum intensity latitude (Fig. 7f). The intensity change is also very mild. In summary, we conclude that the equatorial position of the F_{min} in archeomagnetic field models is not a low resolution effect of these models.

3.2 Surface intensity minima in numerical dynamos

In our dynamo simulations we explored the range of $E = 3 \times 10^{-5}$ to 3×10^{-4}, Ra and Pm values were selected within the dipole dominated non-reversing regime, while q^* was limited to moderate values up to unity to avoid violating the Boussinesq approximation (Table 1). The time-average relative dipole field strength f_{dip} ranges from 0.39 to 0.82 among the dynamo models, while for the geomagnetic field model CHAOS5 $f_{dip} = 0.63$ (Table 2). The mean number of surface intensity minima per snapshot N_F varies from 1.90 to 2.77 (Table 1), in decent agreement with the geomagnetic field models (Table 2). Also similar to the geomagnetic field models, dynamo models rarely have snapshots with a single F_{min}. It is worth noting that the homogeneous heat flux cases have rather large N_F values (Table 1).

Fig. 8 shows two persistent peaks in longitude for most dynamo models with heterogeneous CMB heat flux. This is expected because the lower mantle tomography model is dominated by a Y_2^2 spherical harmonic (Masters *et al.* 2000). In dynamo model case 1 with homogeneous CMB heat flux any deviation from uniformity stems from the finite simulation time and should not be considered as preferred longitudes. In most dynamo models with preferred minima a peak near ≈60° W recovers remarkably well the observed

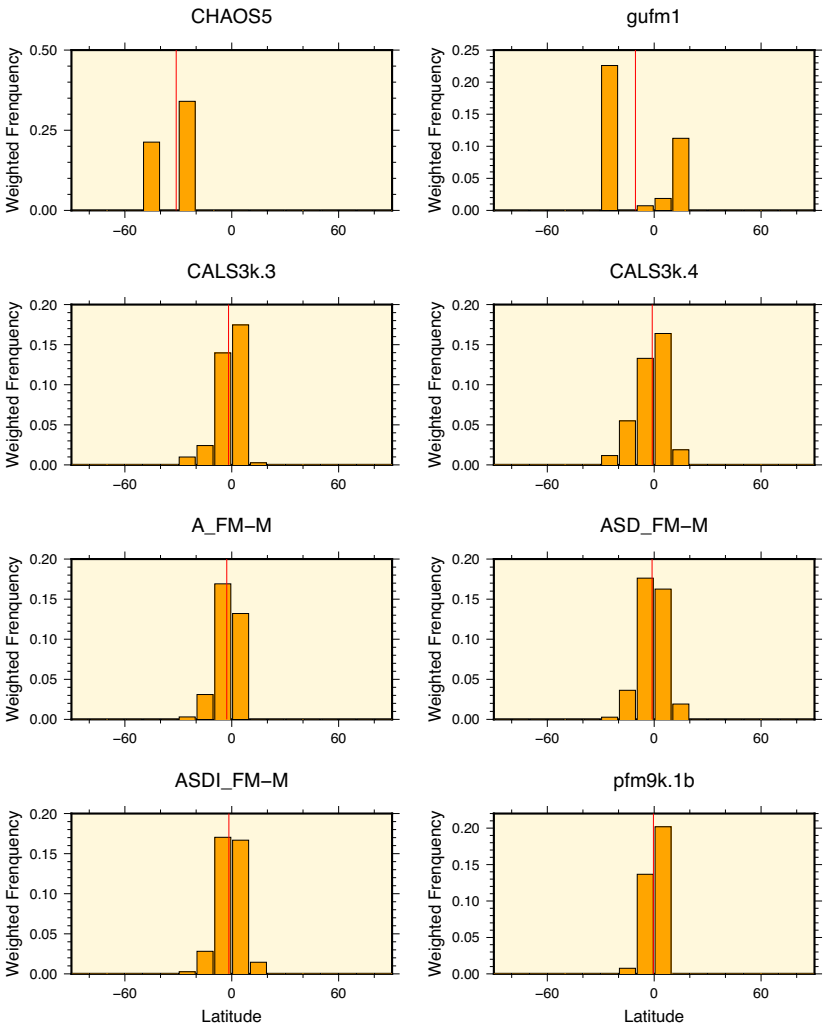

Figure 6. As in Fig. 5 for latitude. Weighted frequency is the integral over time of W_θ (). Red vertical lines denote persistent peaks (15).

geomagnetic field peak at South America (see Fig. 8 and Table 1). The two additional clusters of geomagnetic field peaks at ≈50°E and ≈130°E are reproduced by some numerical dynamo models (see e.g. cases 12 and 13 for the latter), while other dynamo models have peaks in between (compare Tables 1 and 2). Note also that no dynamo simulation exhibits three peaks (Table 1).

In latitude all dynamo models remarkably cluster close to the equator, with $\mathcal{P}_\lambda$ reaching a maximal value of 5.7°S (see case 13 in Fig. 9 and Table 1). This is in striking contrast to the large latitude of the present-day (lowest) minimum intensity at 26°S (Fig. 4b). Note that $\mathcal{P}_\lambda$ in dynamo models, despite being low, tends to the south. In addition, while in the dynamo models a surface intensity minimum at latitude 26°S has a very low probability to occur, Fig. 9 clearly indicates that it is not impossible. The southern tails of some of the peaks indeed encompass such latitudes, for example in cases 8, 12 and 13 in Fig. 9.

3.3 Latitudinal discrepancy

Here we explain the apparent discrepancy between the latitude of F_{min} among the various observed and numerical dynamo models. We search for systematic dependence of λ^*_{Fmin} on the hemispherical distributions of reversed and normal flux on the outer boundary. Fig. 10(a) shows as a typical example the time-dependent f_{dip} values of dynamo model case 6 (solid black line) and its time-average value (horizontal black line). For reference we also show the f_{dip} value of CHAOS5 in 2015 (horizontal blue line). The strong time dependence of f_{dip} of the dynamo model yields some snapshots with a significantly weaker relative dipolar field. In order to avoid non Earth-like morphologies in which the local polarity might not be well defined we exclude from the analysis snapshots with an f_{dip} value smaller than a threshold set to 0.5 (horizontal red line in Fig. 10a).

Fig. 10(b) shows λ^*_{Fmin} (22) versus f_{dip} for the same dynamo model. Note a tendency to the SH. Fig. 10(b) also shows λ^*_{Fmin} versus f_{dip} in the geomagnetic field models CHAOS5 and gufm1. The dipole intensity as well as f_{dip} decrease monotonously from early to recent times (e.g. Finlay 2008). The discontinuities are associated with the λ^*_{Fmin} dependence on the number of F_{min} at each snapshot. In the early period of gufm1 alternations between two and three minima are found, with minima at a given snapshot in both hemispheres, yielding a relatively low λ^*_{Fmin}. After 1980 only one minimum is found, which corresponds to the SAA minimum, hence λ^*_{Fmin} exhibits a jump to the south. In the most recent snapshots of CHAOS5 two minima are found again (e.g. Fig. 4), but this second minimum is now in Africa and further southwards than the SAA,

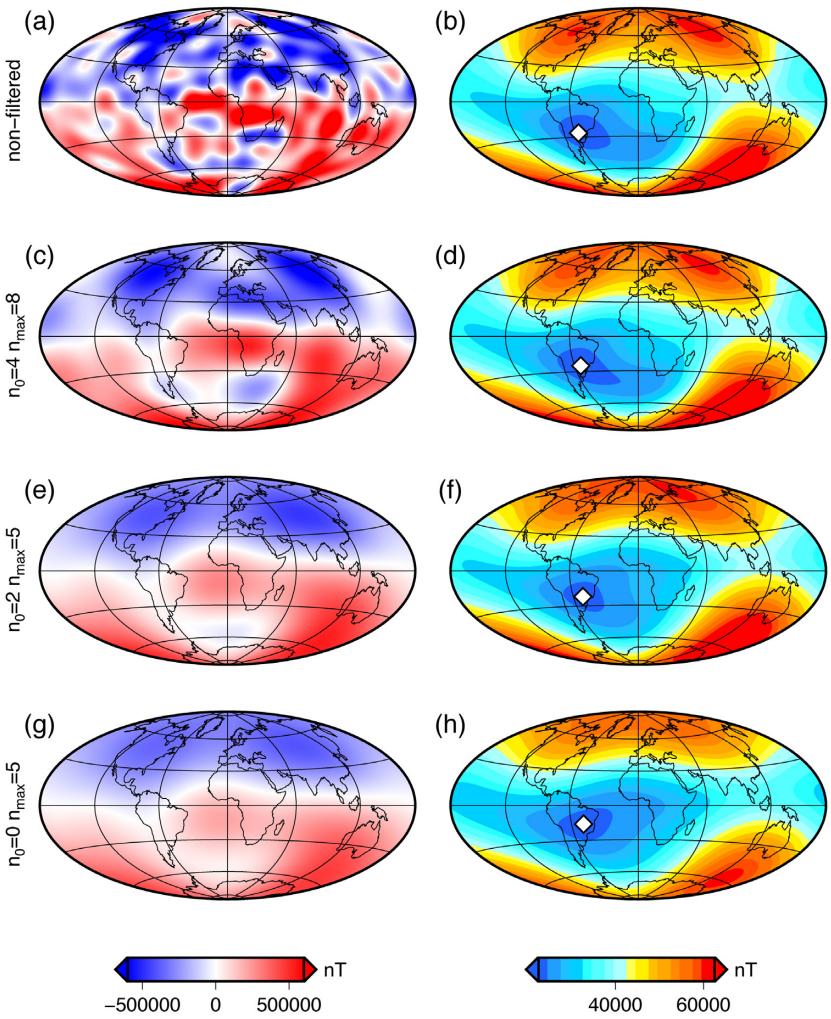

Figure 7. Radial geomagnetic field model CHAOS5 in 2003 at the CMB (left) and intensity at Earth's surface (right) with local intensity minima denoted by white diamonds. Spherical harmonic degrees n_0 and n_{max} indicate low-pass filtering limits (25). The values of [ϕ_{Fmin}, λ_{Fmin} and F_{min}] are [−55°, −26° and 22796 nT], [−54°, −25° and 22680 nT], [−51°, −22° and 23467 nT] and [−49°, −16° and 23319 nT] for (b), (d), (f) and (h), respectively.

hence λ^*_{Fmin} once again exhibits a jump to the south (though this jump is smaller than the previous one).

Most dynamo models have slightly more reversed flux in the NH, that is S^R slightly lower than 0.5 and weak hemispherical asymmetry of reversed flux. In contrast, in the modern and historical geomagnetic field models significantly larger values are found, for example $S^R = 0.72$ at 2015 and $S^R = 0.80$ at 1980, indicating significantly more reversed flux in the SH. Most dynamo models exhibit more normal flux in the NH. The geomagnetic field models also exhibit more normal flux in the NH. Fig. 11 combines the two hemispherical asymmetries for three dynamo models. The negative slopes confirm that indeed often when there is more normal flux in the NH or more reversed flux in the SH the surface minima tends to be in the SH. The proximities of the fitted curves to (0.25,0) confirm that when there are no flux asymmetries, or approximately when the two asymmetries cancel each other out, λ^*_{Fmin} appears at the equator, again as expected. The points are more dispersed from the fitted curve in the lower Ekman number case 28, perhaps due to the shorter simulation time. Overall, the fits explain rather decently the gufm1 results for 1840–1980. However, the present-day large λ^*_{Fmin} is off the fitted curves obtained from the numerical dynamos.

Table 3 shows the linear coefficients for the fits of λ^*_{Fmin} versus hemispherical asymmetries (23) to all dynamo models that have at least 10 per cent of their snapshots with $f_{dip} > 0.5$. Note that all analysed dynamo models show negative slopes a. The interception values of $-b/a$ are very close to 0.25 (Table 3). These results support flux hemispherical asymmetries on the CMB as the determining ingredient for the latitudes of surface intensity minima. However, it is important to keep in mind that these linear curves fit ellipse-like clouds of points in Fig. 11. The limitation of these fits is expressed by the widths of these ellipses.

To demonstrate how the hemispherical asymmetries of the two polarities of the field affect λ^*_{Fmin} we plot in Fig. 12 B_r and $B_r\cos\theta$ at the outer boundary as well as the intensity at Earth's surface for five snapshots from the numerical dynamo models. In Fig. 12(a) there is more normal flux in the NH, while the hemispherical reversed flux asymmetry is much weaker, hence λ^*_{Fmin} is in the SH. In Fig. 12(b) both reversed and normal flux are stronger in the NH thus λ^*_{Fmin} is close to the equator. In Fig. 12(c) the hemispherical flux asymmetries are qualitatively similar to those of Fig. 12(a). However, the lower value of S^{R*} indicates stronger reversed flux in the NH (especially at the north pole), thus F_{min} appears closer to the equator. In Fig. 12(d) the hemispherical normal flux asymmetry again renders

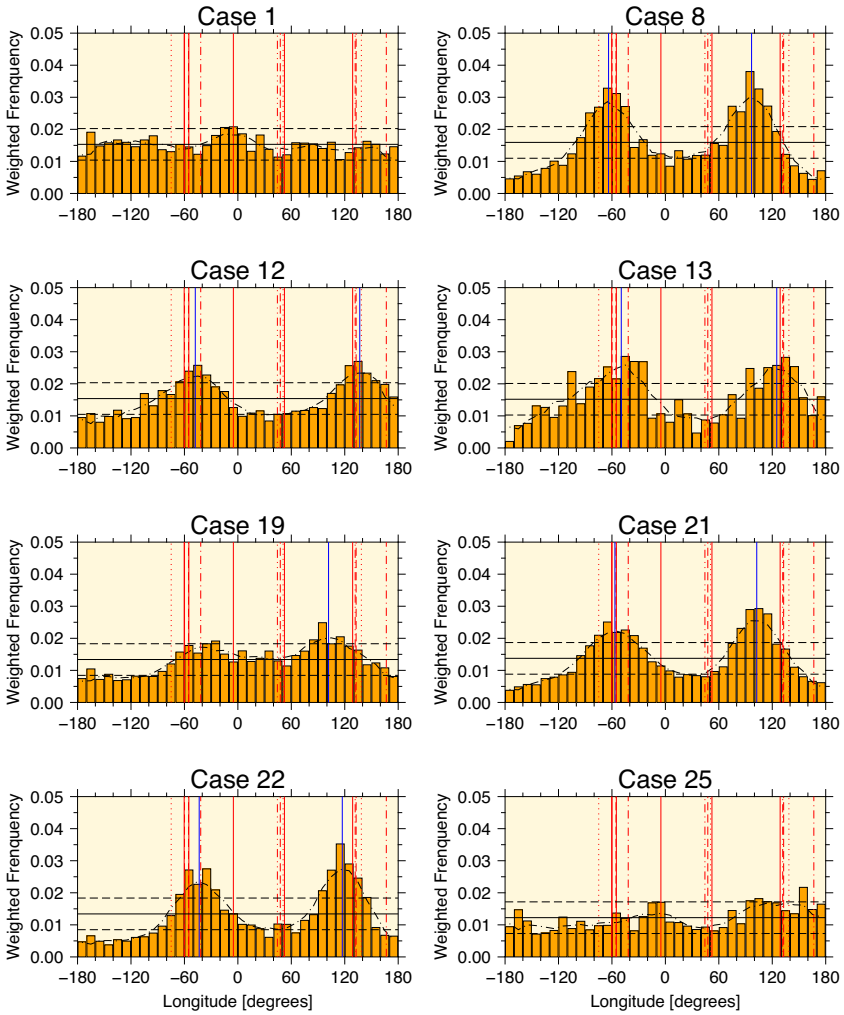

Figure 8. Histograms of local surface intensity minima in longitude for eight dynamo models. Weighted frequency is the integral over time of W_ϕ (12). The histograms are constructed with 10° bins. Blue vertical lines denote persistent dynamo models peaks. Red vertical lines denote geomagnetic field models peaks (Fig. 5), with each line style corresponding to another geomagnetic field model: CHAOS5 (solid), gufm1 (dotted–dashed), CALS3k.4 (dotted–dotted–dashed), ASD_FM-M (dashed), ASDI_FM-M (dotted–dotted–dotted–dashed) and pfm9k.1b (dotted). Models CALS3k.3 and A_FM-M which exhibit five peaks were not included here. The solid black horizontal lines denote the average histogram height of each dynamo model. The dashed black horizontal lines denote ±2 typical heights which are defined by the h_W values of the homogeneous dynamo models with corresponding Ekman numbers.

λ^*_{Fmin} in the SH whereas the hemispherical reversed flux asymmetry is close to 0.5 so it has lesser impact on λ^*_{Fmin}. Nevertheless, the large values reached by λ^*_{Fmin} in this snapshot are difficult to explain based on the hemispherical asymmetries alone, and local contributions by specific flux patches must be invoked (Terra-Nova *et al.* 2017). Strong NFPs below North America and South Pacific comprise most of the normal flux. RFPs far from these regions below the South Atlantic and Indian Ocean lead to F_{min} at relatively high latitudes. In Fig. 12(e) the hemispherical normal flux asymmetry favors F_{min} in the NH but the strong hemispherical reversed flux asymmetry favours the SH with the latter contribution being larger due to a strong RFP extending from below south Africa to Antarctica. The large value of λ^*_{Fmin} is therefore explained by S^{R^*} in this snapshot. Lastly, we also show in Fig. 12(f) B_r and $B_r \cos\theta$ at the CMB as well as the intensity at Earth's surface for the gufm1 model in 1980. Here the reversed flux hemisphericity is very strong with large S^R. However, normal flux dominance with small RN yields moderate S^{R^*}. Nevertheless, both asymmetries work in unison to localize F_{min} in the SH, with comparable contributions from normal and reversed flux. This differs from most dynamo models snapshots where the two flux types exhibit opposing contributions to F_{min} in terms of hemispherical asymmetries (e.g. Figs 12a–e).

3.4 Relations among surface intensity minima, fluid flow and outer boundary heat flux

The dynamic origin of the surface minima can be revealed by inspecting the relations among the field, the flow in the shell and the imposed outer boundary heat flux. Figs 13(a) and (b) show the corresponding tangential divergence and the radial vorticity at the top of the free stream for a snapshot from a heterogeneous dynamo model. The flow is chaotic with small-scale structures. The north–south elongated flow structures indicate dominance of rapid rotation. We find that tangential divergence and radial vorticity are correlated in the SH and anti-correlated in the NH, in agreement with previous numerical dynamos studies (Olson *et al.* 2002; Amit *et al.* 2007; Peña *et al.* 2016). The flow structures are thin,

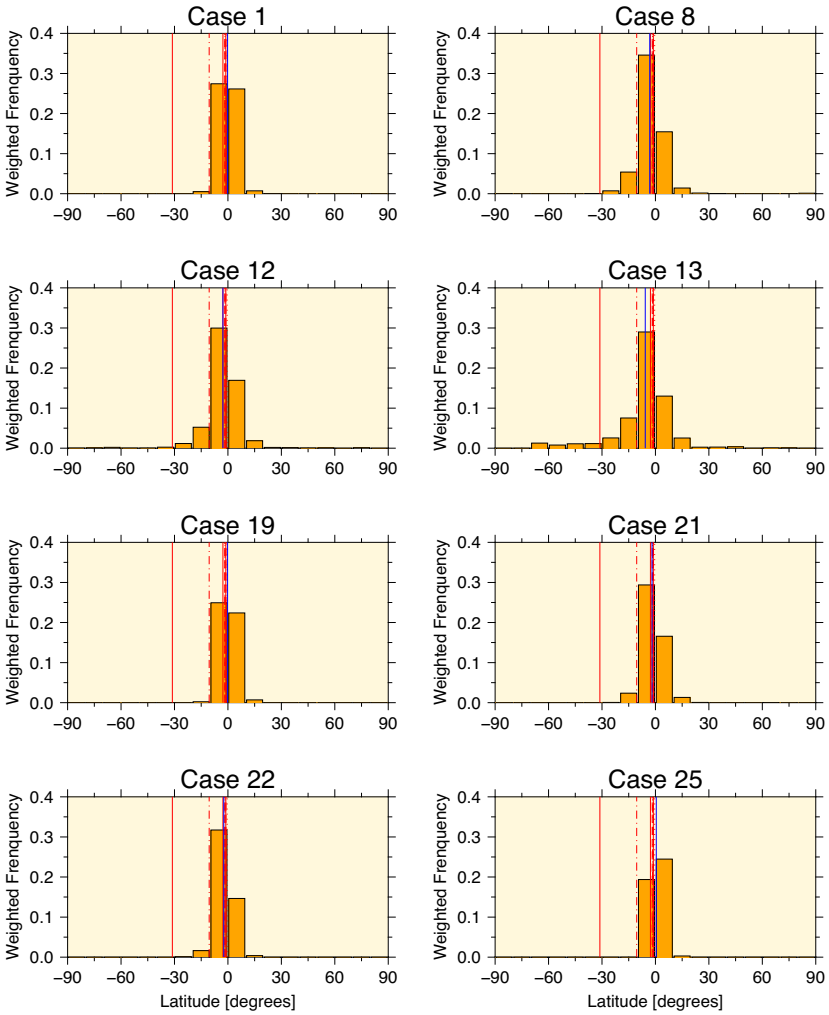

Figure 9. As in Fig. 8 for latitude. Weighted frequency is the integral over time of W_θ (). Blue vertical lines denote persistent peaks (15).

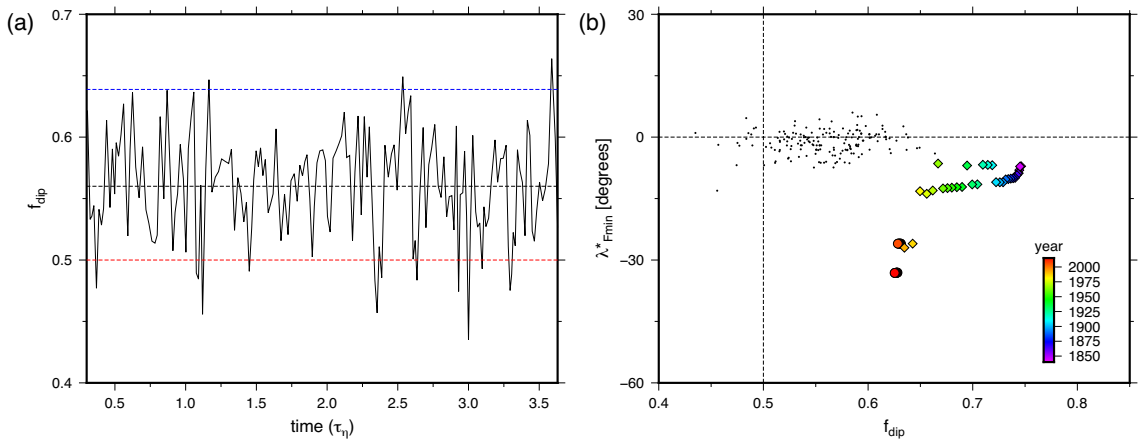

Figure 10. (a) f_{dip} of a dynamo model (case 6) versus time (in units of magnetic diffusion times). Black horizontal line denotes the time-average f_{dip}, red horizontal line our threshold for dipolar regime and blue horizontal line the f_{dip} of CHAOS5 at 2015. (b) Weighted average latitude of the local intensity minima λ^*_{Fmin} versus relative dipole strength f_{dip} for each snapshot of the same dynamo model. Coloured circles and diamonds represent the results for the geomagnetic field models CHAOS5 and gufm1, respectively. Colour scale indicates year.

distributed sporadically over the spherical surface, and are strongly time-dependent. Figs 13(c) and (d) show the corresponding time-average plots. The time-average tangential divergence and radial vorticity are also correlated, thus helical flow (Amit & Olson 2004) holds on long-term time-averages. The boundary signature is clearly evident in the form of two large positive and two large negative flow structures at mid latitudes of both hemispheres (especially in the SH), as expected from the dominant Y_2^2 coefficient in the imposed

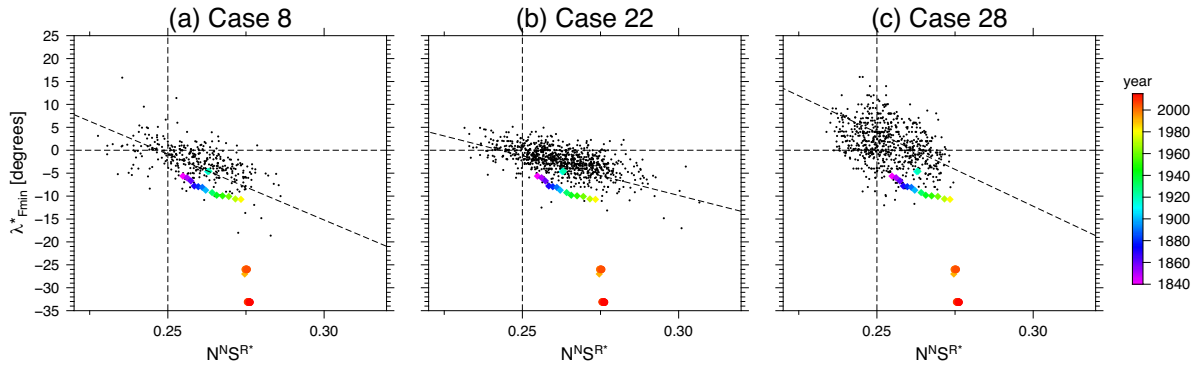

Figure 11. Weighted average surface minima latitude λ^*_{Fmin} versus magnetic flux hemispherical asymmetries on the CMB for three dynamo models. Each point represents a snapshot with $f_{dip} > 0.5$. Coloured circles and diamonds represent the results for the geomagnetic field models CHAOS5 and gufm1, respectively. Colour scale indicates year.

Table 3. Linear fit coefficients of λ^*_{Fmin} versus reversed and normal flux hemispherical asymmetries (23).

Case	a	$-b/a$
2	−224	0.254
3	−254	0.248
4	−371	0.256
5	−343	0.254
6	−171	0.246
7	−299	0.244
8	−287	0.247
9	−436	0.264
12	−279	0.251
13	−176	0.233
14	−155	0.252
15	−274	0.259
16	−390	0.262
17	−520	0.256
18	−423	0.255
19	−125	0.248
20	−201	0.254
21	−204	0.245
22	−173	0.243
24	−149	0.235
25	−277	0.260
26	−46	0.283
27	−78	0.256
28	−321	0.262

a is the slope, $-b/a$ is the interception with λ^*_{Fmin}=0.

heat flux boundary pattern (Masters *et al.* 2000). Preferred longitudinal positions of downwellings appear close to longitudes of positive heat flux anomalies strips (see Fig. 1 for illustration and Fig. 2 for the imposed tomographic pattern). We find a strong persistent region of upwelling below the South Atlantic extending from Africa to South America (Fig. 13c), which is responsible for the expulsion of toroidal field lines and emergence of reversed magnetic flux at the outer boundary. In the time-average flow images of the homogeneous dynamo model (Figs 13e and f) as expected no such longitudinal preference appears (as in e.g. Olson & Christensen 2002).

Fig. 14(a) shows the zonal velocity profile for a snapshot from the same heterogeneous dynamo model (case 13). At low and mid latitudes westward flow prevails in the SH and eastward flow in the NH. In the long-term time-average images of the same dynamo model (Fig. 14b) the morphology of the velocity field is characterized by fewer and larger scale convective cells. The westward/eastward flow outside the tangent cylinder is again mostly in the SH/NH, respectively. Downwellings are found at the edges of the tangent cylinder and upwellings dominate polar regions. The downwellings on the tangent cylinder are stronger in the NH, yielding stronger magnetic flux in the NH than in the SH. For reference, Fig. 14(c) shows the long-term time-average from a homogeneous dynamo model. In the absence of boundary heterogeneity, the zonal velocity profile is perfectly equatorially symmetric without any north–south asymmetry.

Can the southern tendency of the surface intensity minima (Fig. 6 and Table 1), the enhanced magnetic activity in the NH (Figs 11 and 12) and the enhanced convective activity at the top of the shell in the NH (Fig. 14) be explained by north–south asymmetry in the outer boundary heat flux of the dynamo models? In Fig. 15 we show longitude integrated heat flux versus latitude. The heat flux in the NH is dominated by stronger than average values whereas the SH is largely dominated at low and mid latitudes by weaker than average heat flux (see also Amit & Olson 2006). The stronger than average integrated heat flux at high latitudes of the SH corresponds to a small area. Thus the NH is characterized by a larger heat flux leading to more convective and magnetic activities than in the SH. The production of stronger mantle driven NFPs in the NH renders the surface minima to the SH.

3.5 Dependence on dynamo parameters

Here we derive scaling laws using the dynamo control parameters. We consider scaling laws for the persistence of surface intensity minima and for their coordinates. The fits are obtained using a conventional least squares method (as in Peña *et al.* 2016).

The persistence of recurrent positions of F_{min}, expressed by h_W, is best fitted by the following power law:

$$h_W \approx 0.16 E^{0.83} Ra^{0.27} Pm^{-0.17} q^{*0.45}. \quad (26)$$

Because h_W should vanish if the heat flux is homogeneous we excluded in (26) the homogeneous cases and forced interception at (0,0). Fig. 16 shows h_W for the dynamo models along with the acquired power law fit. Faster rotation (which stabilizes the dipole) acts against preferred longitudinal positions, while stronger boundary-driven flow due to larger values of q^* favors preferred longitudinal distribution. The intermediate positive power of Ra indicates that increased main convection vigor also strengthens h_W though to a lesser extent, while Pm has the smallest effect. Overall, the strongest sensitivity of h_W is to E.

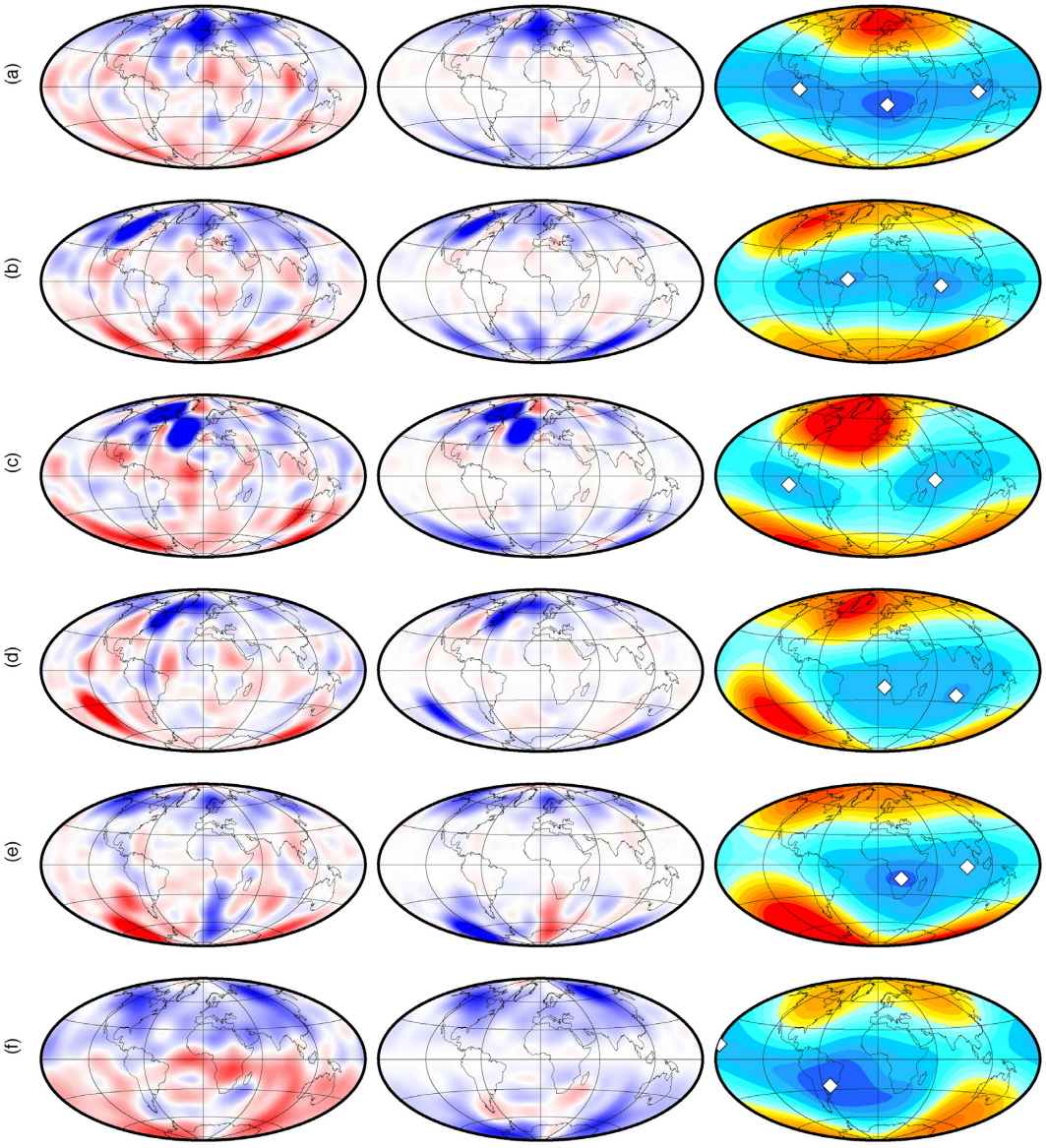

Figure 12. Radial field on the CMB truncated at $n_{max} = 14$ (left), spatial contribution to the axial dipole (middle) and surface intensity at Earth's surface (right) for five snapshots from numerical dynamos (a-e) and gufm1 in 1980 (f). White diamonds (right) denote the identified intensity minima. The values of $[N^N, S^{R^*}$ and $\lambda^*_{Fmin}]$ are [0.59, 0.48, −8.79°], [0.52, 0.49, −1.14°], [0.58, 0.46, −5.94°], [0.56, 0.49, −20.64°], [0.47, 0.56, −9.44°] and [0.52, 0.52, −10.72°] for (a)-(f), respectively. All snapshots are from case 7, expect for (c) from case 10.

The dependence of the longitude of the most persistent (Western Hemisphere) peak $\mathcal{P}_{\phi 1}$ (Table 1) on the control parameters follows

$$\mathcal{P}_{\phi 1} \approx 29 E^{1.37} Ra^{0.75} Pm^{-0.10} q^{*0.14} - 98. \quad (27)$$

Fig. 17 shows the fit for $\mathcal{P}_{\phi 1}$. Rotation has the strongest impact, with Ra less influential. The slope is positive and E and Ra have positive powers, that is the surface minima are shifted westward when rotation is faster and convection is weaker. Other longitude peaks do not appear in sufficient dynamo models, hence lack meaningful statistics for deriving additional scaling laws as in (27). Even in the case of Fig. 17 the number of points might not be satisfactory to properly constrain the powers of the scaling law (27).

The dependence of latitudinal peaks $\mathcal{P}_\lambda$ on the dynamo control parameters is best fitted by the following power law

$$\mathcal{P}_\lambda \approx -8740 E^{5.67} Ra^{2.53} Pm^{0.07} q^{*1.48}. \quad (28)$$

As in (26) P_λ is expected to be zero (i.e. at the equator) in the homogeneous case, thus in (28) these cases are excluded and the fit is forced to intercept (0,0). Fig. 18 shows the fitted power law. Here rotation is the most influential while Ra and q^* have a weaker effect. As in (26)–(27) the effect of Pm is negligible. The negative slope and the positive powers indicate preference to minima in the SH when rotation is slower, convection is stronger and the boundary heterogeneity is larger.

Higher latitudes of surface intensity minima occur in dynamo models with more persistent longitude peaks. Fig. 19 shows the relation between $\mathcal{P}_\lambda$ and h_W. Weak mantle control gives small h_W, one surface minimum or none (Table 1) and somewhat non-intuitively northern tendency (though weak). Further increase in h_W gives two surface minima (Table 1) and increasingly southward surface minima (Fig. 19). This same qualitative relation also holds for the geomagnetic field models (see red diamonds in Fig. 19).

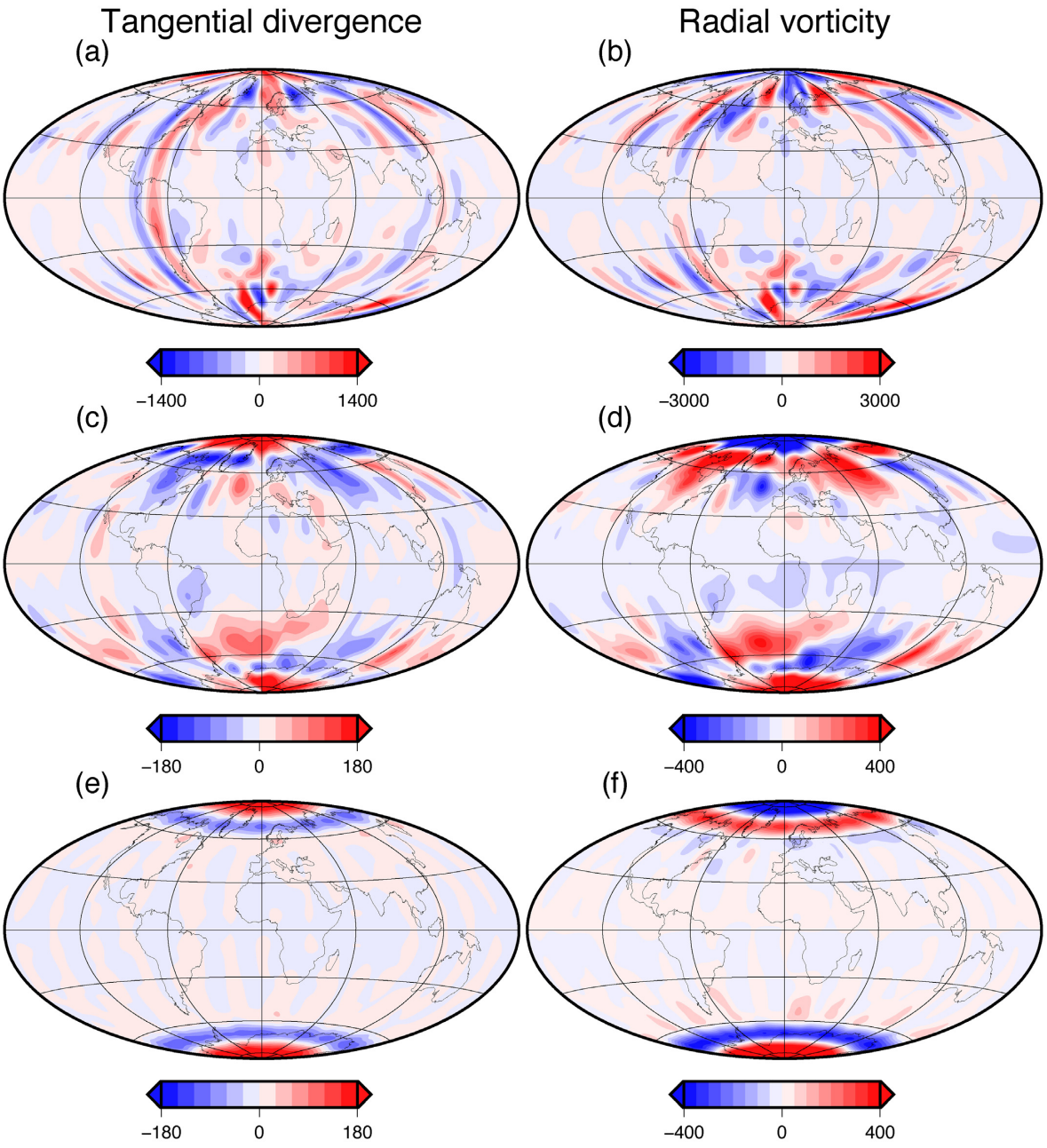

Figure 13. Tangential divergence (left) and radial vorticity (right) at the top of the free stream just below the Ekman boundary layer for a snapshot of heterogeneous dynamo model case 13 (a and b), time-average of the same dynamo model (c and d) and time-average of homogeneous dynamo model case 1 (e and f).

4 DISCUSSION AND CONCLUSIONS

The identification of local surface intensity minima in geomagnetic field models reveals at present two minima (Fig. 4) and that overall it is rather rare to find only one minimum in a snapshot (Table 2). The morphology of the SAA is therefore more complex than often thought, which might lead to some misinterpretations. For example, ignoring the existence of multiple surface minima might lead to discontinuous tracking of the absolute minimum. In addition, attempts to identify the SAA using regional archeointensity time-series (Tarduno *et al.* 2015; Shah *et al.* 2016) might erroneously ignore the existence of additional minima. Nevertheless such local time-series may be useful in detecting shallow surface minima that are otherwise non-detectable in strongly regularized global field models. For example, when applying a low-pass filter (25) to the CHAOS5 model at 2015 (Fig. 4), the minimum intensity at South America is still found, but the Africa minimum disappears, that is the existence of the present surface minimum in Africa is strongly dependent on the small scales.

Among the geomagnetic field models there is agreement in persistent longitudes of local surface intensity minima, most notably for the peaks around 60°W, close to the present-day prominent SAA minimum at ∼56°W (Terra-Nova *et al.* 2017). Overall, three clusters of longitudinal positions are found in the geomagnetic field models (see Fig. 5 and red vertical lines in Fig. 8). In contrast, there is a substantial difference among the geomagnetic field models in

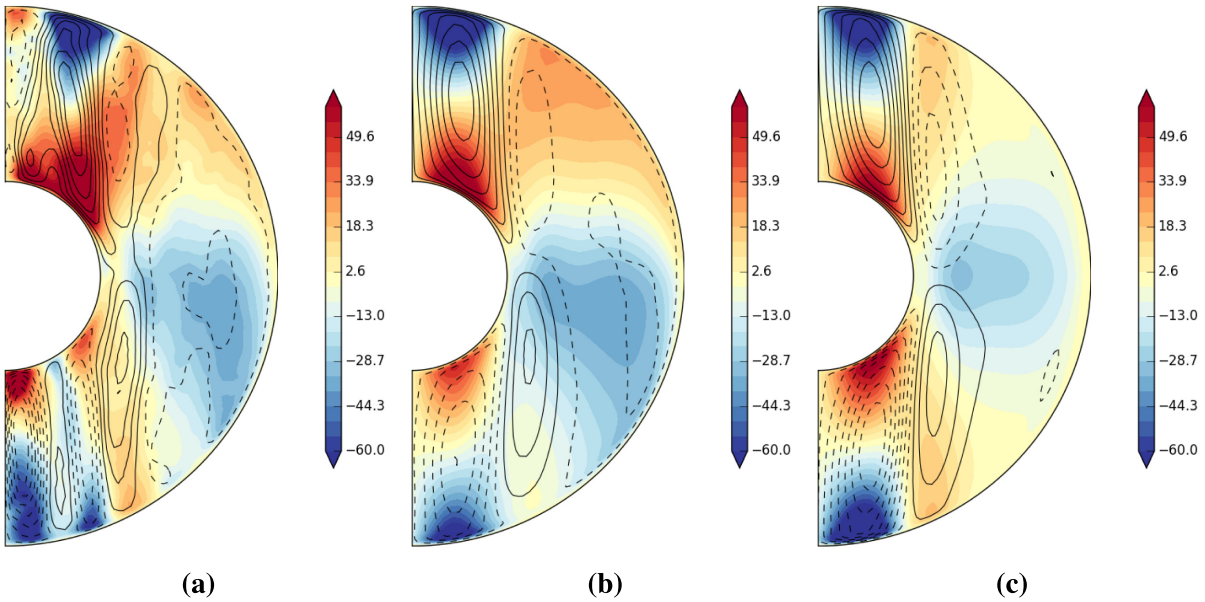

Figure 14. Zonal velocity (colours) and meridional circulation (contours) for (a) a snapshot from a heterogeneous dynamo model, (b) time-average of the same model and (c) time-average of a homogeneous outer boundary heat flux dynamo model. Red/blue denotes eastward/westward, solid/dashed denotes clockwise/anticlockwise circulation. The cases are the same as in Fig. 13 .

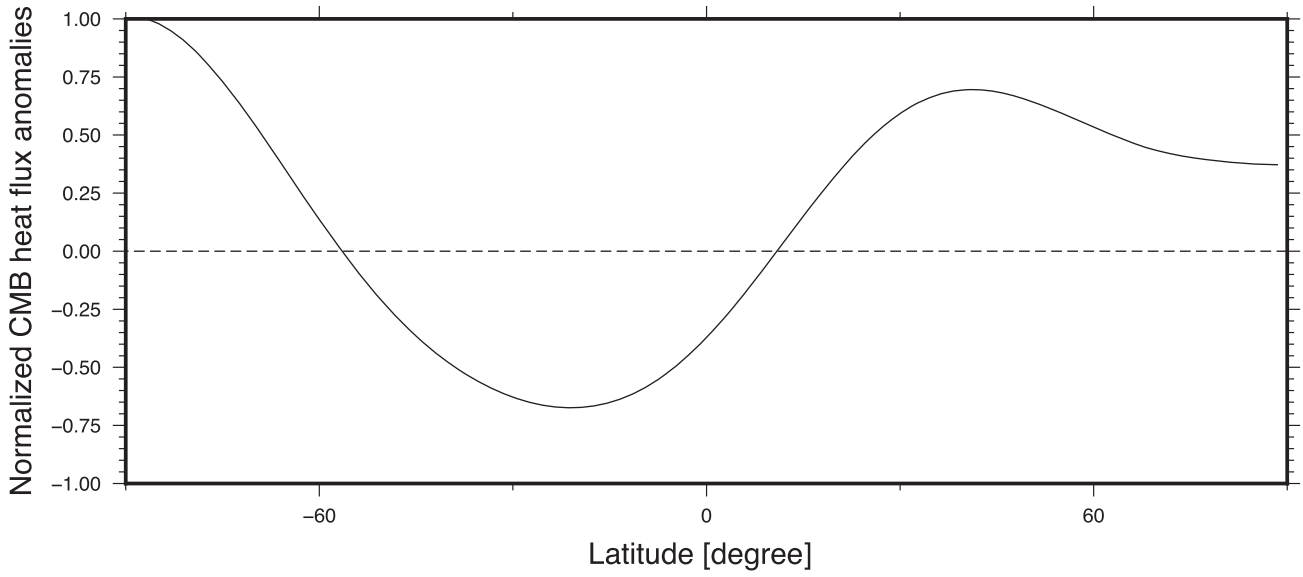

Figure 15. Normalized longitude integrated CMB heat flux anomalies of the tomographic model shown in Fig. 2.

the latitude distributions. The modern and historical geomagnetic field models contain mid-latitude local intensity minima, whereas in archeomagnetic field models the minima are clustered on the equator (Fig. 6). The results of the sensitivity test (Fig. 7) suggest that the equatorial location of F_{min} in archeomagnetic field models is not a consequence of their low resolution. However, caution is required when interpreting this test because it lacks information about the projection of the spectral resolution on to grid space. Hellio & Gillet (2018) showed that the spatial resolution of the surface intensity strongly varies between the NH and SH (see their Fig. 11). The highly uncertain and geographically sparse archeomagnetic database (e.g. Donadini *et al.* 2009; Brown *et al.* 2015a,b) used to reconstruct these field models (e.g. Korte *et al.* 2009; Licht *et al.* 2013; Nilsson *et al.* 2014) limits their reliability. These issues are partially overcome by different data treatments and modeling strategies (for details see section 2 of Terra-Nova *et al.* 2016). However if the true latitude of F_{min} during the Holocene is indeed biased by these quality issues then random latitudes are expected, not necessarily the equator.

Persistent longitudes of magnetic local surface intensity minima in numerical dynamo simulations with imposed heterogeneous heat flux are clearly seen by histogram peaks (Fig. 8) and quantified by typical peaks height h_W (Table 1). Two longitudinal preferred positions are recovered by most of the dynamo simulations, consistent with the dominant Y_2^2 signal in the heterogeneous CMB heat flux pattern (Masters *et al.* 2000). One of these peaks recovers well the persistent peak in the geomagnetic field models at the present day SAA absolute minimum. It is important to emphasize that it

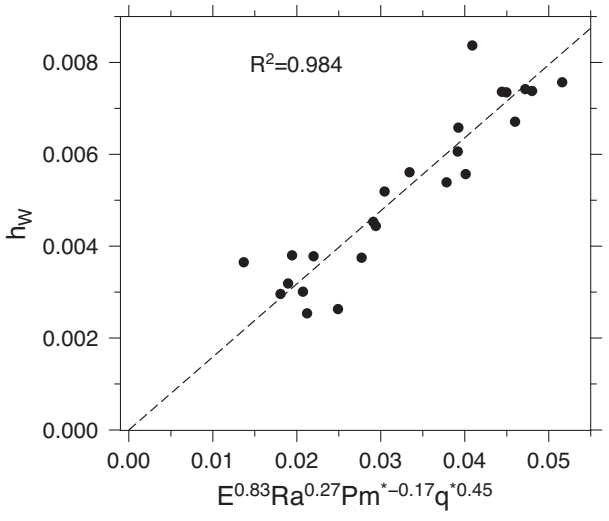

Figure 16. Scaling law for the typical height h_W, which measures the persistence of surface intensity minima peaks. The goodness of fit is measured by R^2.

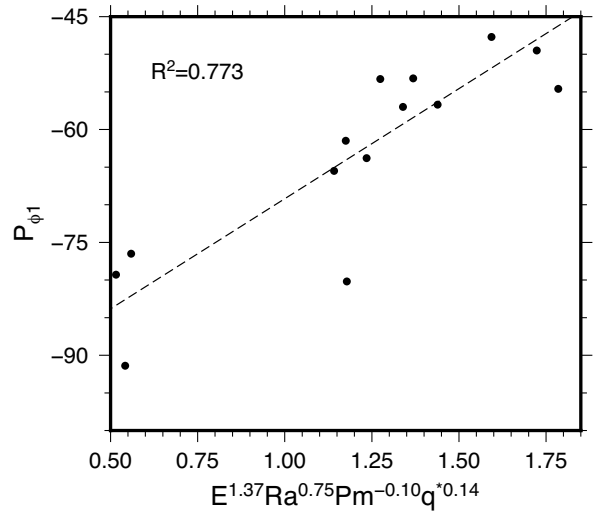

Figure 17. As in Fig. 16 for the longitude of the Western peak of local minima of surface intensity.

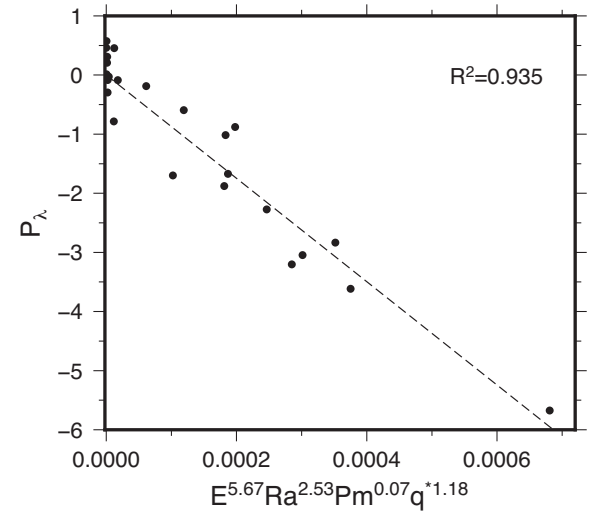

Figure 18. As in Fig. 16 for the latitudinal peak of local minima of surface intensity.

does not imply that the weak surface intensity field is locked to South America. Surface intensity minima are found at all longitudes in the dynamo models (Fig. 8). Instead, these histogram peaks mean that the CMB heat flux heterogeneity yields statistical preference for some weak surface intensity locations within a strongly time-dependent system (e.g. Olson & Christensen 2002; Amit *et al.* 2010).

Various SV scenarios may be envisaged to explain the preferred longitudes of surface minima. One possibility is that the flow is slower in these regions hence RFPs reside longer there. However, core flow models from SV inversions show a more active Atlantic Hemisphere where the SV is stronger (Jackson 1997; Hulot *et al.* 2002; Amit & Olson 2006; Holme & Olsen 2006; Aubert & Fournier 2011; Aubert *et al.* 2013; Gillet *et al.* 2015) therefore this scenario is not appealing. Alternatively, preferred locations of fluid upwellings may lead to preferred locations of flux expulsion at the top of the core and weak surface intensity at nearby coordinates. We hypothesize that significant radial diffusion associated with core fluid upwelling (Amit & Christensen 2008; Barrois *et al.* 2017) is needed to explain the preferred longitudes of weak surface intensity.

The discrepancy between surface intensity minima of modern and historical field models at mid-latitudes to those of the dynamo models near the equator could possibly be related to non Earth-like features of the numerical dynamo models. However, the latitude of the surface intensity minima in the dynamo models is in agreement with archeomagnetic field models. It could be argued that the equatorial position of persistent minima in the archeomagnetic field models is due to their low resolution. However, the dynamo models have a much higher resolution than any observations based geomagnetic field model. We elaborate below on why dynamo simulations seldom reproduce the present latitude of the SAA.

We investigated the role of reversed and normal flux at the CMB in determining the latitude of the surface intensity minima. We quantified the hemispherical asymmetries of the two flux types. More reversed flux in one hemisphere renders F_{min} in the same hemisphere, whereas normal flux has the opposite effect (Terra-Nova *et al.* 2017, fig. 3). The F_{min} latitudes are more sensitive to the hemispherical asymmetry of the more abundant normal flux. Applying a proper normalization to the reversed flux hemisphericity based on its relative strength (21), we demonstrated how these two flux ratios affect the latitude of F_{min} (Figs 11 and 12). Our numerical dynamo simulations lack systematic strong north–south asymmetry of reversed flux. Thus the present latitude of the SAA is rarely recovered in the dynamo models. We speculate that the present-day extensive SH geomagnetic reversed flux and consequently the relatively high latitude of the SAA are possibly rare characteristics of the Earth's magnetic field. In particular, while the historical field is in decent agreement with the dynamo models in terms of the relation between surface minima latitude and flux hemisphericities, the modern field is off the linear regressions (Fig. 11).

The tendency to equatorial surface minima in our dynamo models may be alternatively explained by control parameters that are orders of magnitude away from Earth-like values. However, this seems unreasonable, because the Ekman number of Earth's core is much smaller favoring a stronger tendency of surface minima towards the equator (Fig. 19). Alternatively, the CMB heat flux might be wrong because it relies on an oversimplified lower mantle seismic-thermal relation (Amit *et al.* 2015a). Here we chose to use the tomography model of Masters *et al.* (2000) for several reasons. First, this model has been used by numerous studies of numerical dynamos (e.g. Aubert *et al.* 2008). Second, inferring a non-linear

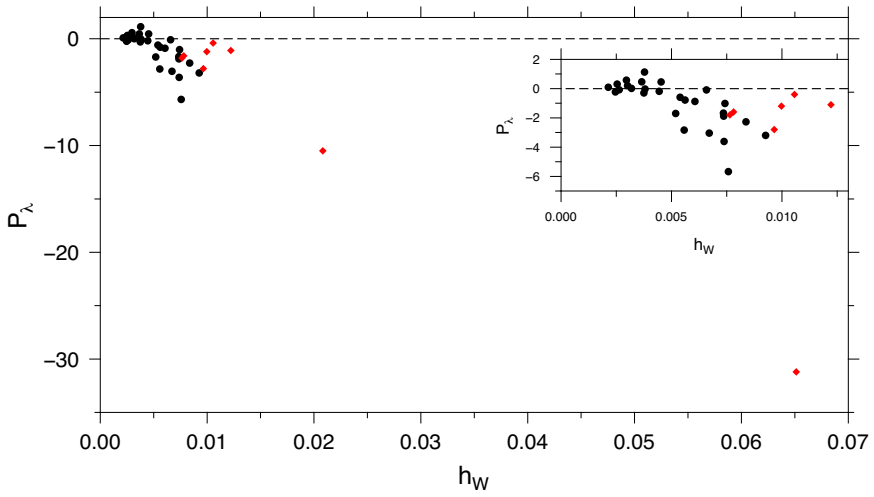

Figure 19. Persistent latitude of local minima of surface intensity versus the typical height h_W that measures the persistence of surface intensity minima peaks. Black circles are dynamo models, red diamonds are geomagnetic field models. The inset is a zoom into the region of numerical dynamo and archeomagnetic field models.

thermal anomaly from the seismic anomaly is still highly debated (Amit *et al.* 2015a). Finally, the model of Masters *et al.* (2000) is in agreement with the large-scale features of most lower mantle tomography models (Lekic *et al.* 2012). We note that the tomography model of Masters *et al.* (2000) contains more positive anomalies in the NH (Fig. 15), leading to more convective and magnetic activities in that hemisphere. In contrast, paleosecular variation index values (Panovska & Constable 2017) and hemispheric asymmetry in the Holocene (Constable *et al.* 2016) are evidence for more field activity in the Southern Hemisphere. Amit & Choblet (2012) imposed narrow hot ridges separating large-scale positive and negative seismic anomalies on their dynamo models. They found that these hot ridges lead to core fluid upwelling and a barrier for azimuthal flow. East of these ridges persistent intense geomagnetic flux patches are expected. Amit *et al.* (2015b) imposed on their dynamo models a CMB heat flux from the thermal component of the probabilistic tomography model of Mosca *et al.* (2012). They found that the dynamo models with a probabilistic tomography CMB heat flux have more low-latitude convective and magnetic activities than corresponding models with conventional tomographic heat flux, and thus may recover the observed latitudinal distribution of geomagnetic flux on the CMB. Although these studies are not yet converging, it is nevertheless worth considering alternative CMB heat flux models based on dynamic scenarios of the lower mantle.

Next we investigated the dynamic origin of the surface intensity minima, that is the relation between the imposed heterogeneous outer boundary heat flux, the flow inside the shell and the surface intensity minima in the numerical dynamo simulations. The westward/eastward flow outside the tangent cylinder that prevails in the SH/NH respectively on time-average in the heterogeneous heat flux dynamo models already appears in snapshots (Figs 14a and b). This shows that the signature of the boundary heterogeneity on the zonal flow is very persistent, that is its effect is more than that of merely a statistical preference. The tangential flow at the top of the free stream reflects clearly the heterogeneous heat flux pattern. The flow is concentrated in the Atlantic Hemisphere with a quieter Pacific Hemisphere (Figs 13b and d), in agreement with the geomagnetic SV on various timescales (e.g. Bloxham 1989; Hulot *et al.* 2002; Gubbins & Gibbons 2004; Holme *et al.* 2011; Aubert *et al.* 2013). Positive CMB heat flux anomalies are expected to yield downwellings and intense NFPs (Gubbins 2003) whereas negative heat flux anomalies may give upwellings, RFPs (Terra-Nova *et al.* 2016) and persistent regions of weak intensity at the surface. The persistent upwelling at the South Atlantic in Fig. 13(c) is a particularly relevant example for such a relation. In this region expulsion of toroidal field lines leads to reversed flux and a preferred location for weak surface intensity, in agreement with the current extent of the SAA region. This South Atlantic upwelling is a persistent feature in most of our dynamo models with heterogeneous CMB heat flux inferred from lower mantle tomography. Using RFPs in an archeomagnetic field model, large persistent upwelling structures of $80^\circ - 110^\circ$ were inferred (Terra-Nova *et al.* 2016), of about the same size as the large time-average upwelling below the South Atlantic in Fig. 13(c). The corresponding South Atlantic vortex (Fig. 13d) may explain the breaking of equatorial symmetry of advective sources of axial dipole moment in the historical field below South America (Finlay *et al.* 2016).

Persistent deviations from equatorial symmetry or from axisymmetry can also appear with homogeneous boundary conditions. Landeau & Aubert (2011) showed that a hemispheric (northern or southern) convective mode emerges for a thermally driven dynamo without an inner core when convection is very strong. They proposed that such a convective mode may explain the south–north dichotomy in Mars' crustal field. Schaeffer *et al.* (2017) showed that a numerical dynamo with relatively vigorous convection, rapid rotation and low viscosity produces westward drift of magnetic field features in one (eastern or western) hemisphere. However, the above mentioned correlations of lowermost mantle seismic heterogeneity with the specific positions of geomagnetic flux patches on the CMB (Gubbins 2003; Gubbins *et al.* 2007; Terra-Nova *et al.* 2016) suggest that mantle control is more likely to explain these features. In addition, even if some hemispherical convective mode naturally emerges (as in Landeau & Aubert 2011; Schaeffer *et al.* 2017), CMB heat flux heterogeneity may strengthen it and select its phase (i.e. northern or southern, eastern or western).

Hemispherical asymmetry is clearly seen in the CMB heat flux model (Fig. 15). The NH has more positive heat flux, which affects the flow morphology. Fig. 14(b) shows that the low-latitude westward flow is pushed southwards due to the hemispherical asymmetry of the heat flux. Stronger convective activity in the NH, in

particular stronger downwelling at the tangent cylinder (Fig. 14b), results in stronger magnetic activity in the NH.

The choice of dynamo control parameters is limited by the applicability of our models. For a given E, too strong forcing (large Ra and q^*) might lead to reversing dynamos with non-dipolar morphologies. In the other limit, too weak forcing gives too weak mantle control effects. Increasing Pm stretches the range of Ra for dipole-dominated dynamos (Christensen & Aubert 2006) but renders the simulation too slow in terms of magnetic diffusion times. In addition we limited q^* to unity in order to avoid violating the Boussinesq approximation on which the dynamo models rely. Nevertheless our dynamo models cover some variability of the control parameters within the above constraints.

The level of persistence of preferred longitudes of surface minima is quantified by h_W (Table 1). Stronger rotation effects (smaller E) yield more uniform longitudinal distribution of surface intensity minima over time. Persistent longitudes of surface minima arise when convection is increased (larger Ra) and especially when boundary heterogeneity is increased (larger q^*), as expected. Note that the fitted power of q^* is nearly a factor two larger than that of Ra. The dependence on Pm is the weakest.

Experiments of non-magnetic rotating thermal convection with heterogeneous localized outer boundary heat flux found that the downwelling is strongly shifted westward of the large outer boundary heat flux region (Sumita & Olson 1999, 2002). Numerical dynamos with a Y_1^1 outer boundary heat flux pattern exhibited a surprisingly large shift of ∼180 degrees between the large heat flux region and the time-average intense flux patch on the outer boundary (Amit & Olson 2015). Previous studies of numerical dynamos with a Y_2^2 outer boundary heat flux pattern generally found more moderate shifts between the two longitudes of maximum anomalies and the two longitudes of time-average high-latitude intense magnetic flux patches, with the determining parameter for the size of the shift being debated (Olson & Christensen 2002; Aubert *et al.* 2007; Takahashi *et al.* 2008). Our approach and applicability differ in several aspects. First, we explored a set of dynamo models with multiharmonic tomographic outer boundary heat flux. Second, we analysed long time-series of snapshots (as in Amit *et al.* 2010) rather than time-averages. Finally, we studied persistent surface intensity minima (rather than intense outer boundary flux patches) with the SAA in mind.

We found that the surface minima are shifted westward when rotation is faster, convection is weaker and the boundary heterogeneity is stronger (Fig. 17). The surface minima appear further from the equator to the south when rotation is slower, convection is stronger and boundary heterogeneity is larger (Fig. 18). While this dependence of the latitude of the surface minima on the dynamo control parameters is qualitatively somewhat expected, the relative powers unravelled by the scaling laws analysis may provide interesting insights. For example, note that the ratio of E exponent over q^* exponent in (26) is more than twice larger than in (28). This demonstrates the larger sensitivity of longitude to mantle control than that of latitude, further supporting our choice of separate analyses for longitude and latitude.

Extrapolation of the scaling laws to Earth-like control parameters gives $\mathcal{P}_\lambda = 0$. It is important to keep in mind that the ranges of h_W and in particular $\mathcal{P}_\lambda$ are so small that such extrapolations are not robust. The sensitivities of the scaling laws to the powers are very large. We therefore mostly focus on interpretations of the signs and relative sizes of these powers rather than their specific values. Nevertheless, the extrapolated $P_\lambda = 0$ value is in agreement with the results for the archeomagnetic field models. In this context it is worth recalling the way P_λ is calculated and what it represents. First, it is a time-average quantity, that is the equator is the most probable location of the surface minima in an axial dipole dominated field. However, there are snapshots when P_λ reaches the latitude of the present geomagnetic field (Fig. 9), consistent with the SAA latitude being rare though possible. Second, at any snapshot P_λ is the weighted average of all surface minima (15). In some dynamo model snapshots a surface minimum is found in a relatively high latitude but it is counter-balanced by other surface minima that reside either in the other hemisphere or at low latitudes. It is therefore possible that the rareness of the present geomagnetic field is not its relatively high latitude SAA but rather the absence of other surface minima to balance it in the Northern hemisphere or at the equatorial region. Indeed, note that the number of surface minima in CHAOS-5 is less than two, whereas in the other geomagnetic field models as well as in the dynamo models $N_F > 2$ (Tables 1 and 2).

The southern latitude of the surface minima $\mathcal{P}_\lambda$ is correlated with persistence of surface minima longitudes h_W in dynamo models (Fig. 19). There is a suggestion for a similar correlation in geomagnetic field models (Fig. 19), although this correlation might be fortuitous due to the short periods of the historical and modern field models. Note that in CHAOS5 and gufm1 the short periods yield non-representative large h_W, and interestingly large $\mathcal{P}_\lambda$ as well. Overall, when mantle control is stronger, that is convection dominates over rotation, the surface minima are more persistent (larger h_W) and more southern (more negative $\mathcal{P}_\lambda$). This may indicate that the southern location of the SAA is mantle controlled, in agreement with some archeomagnetic field models (Brown *et al.* 2018; Hellio & Gillet 2018).

In summary, the dynamo models recover the correct longitude of the SAA surface intensity minima as well as the correct (Southern) hemisphere. The historical field roughly matches the curve of the F_{min} latitude versus flux hemisphericities (Fig. 11). Heterogeneous outer boundary heat flux dynamo models exhibit stronger convective and magnetic activity in the NH. Persistent upwelling at the top of core below the South Atlantic leads to a statistically preferred region of weak surface intensity, in good agreement with the current extent of the SAA. Improved archeomagnetic field models (Hellio & Gillet 2018), progress in extracting the CMB heat flux from seismic tomography models using mantle convection simulations (Choblet *et al.*, in preparation) and exploration of additional numerical dynamo models (Aubert *et al.* 2017) together with the processing schemes proposed here may further improve the understanding of the dynamic origin of the SAA, its relation to the heterogeneous lower mantle and its persistence.

ACKNOWLEDGEMENTS

We are grateful to Maurits Metman and an anonymous reviewer for their constructive comments that improved the manuscript. We thank Guy Moebs for the valuable technical support with the numerical dynamo simulations. Computations were performed on the CCIPL. The source of MagIC (numerical dynamo code) is available at https://magic-sph.github.io/. We thank Thomas Gastine for his support with MagIC 5.6. F. T-N. acknowledges The National Council for Scientific and Technological Development (CNPq/Brazil) for grant 206997/2014-0 and São Paulo Research Foundation (FAPESP) for grant 2018/07410-3. F. T-N. and H. A. were partly supported by the Centre National des Études Spatiales (CNES). This work acknowledges the financial support from Région Pays de la Loire, project GeoPlaNet (convention N° 2016-10982).

REFERENCES

Amit, H., 2014. Can downwelling at the top of the Earth's core be detected in the geomagnetic secular variation? *Phys. Earth planet. Inter.,* **229,** 110–121.

Amit, H., Aubert, J. & Hulot, G., 2010. Stationary, oscillating or drifting mantle-driven geomagnetic flux patches? *J. geophys. Res.,* **115**(B07108), doi:10.1029/2009JB006542.

Amit, H., Aubert, J., Hulot, G. & Olson, P., 2008. A simple model for mantle-driven flow at the top of Earth's core, *Earth Planets Space,* **60,** 845–854.

Amit, H. & Choblet, G., 2012. Mantle-driven geodynamo features - effects of compositional and narrow D" anomalies, *Earth Planet. Inter,* **190-191,** 34–43.

Amit, H., Choblet, G., Olson, P., Monteux, J., Deschamps, F., Langlais, B. & Tobie, G., 2015a. Towards more realistic core-mantle boundary heat flux patterns: a source of diversity in planetary dynamos, *Prog. Earth planet. Sci.,* **2**(26), doi:10.1186/s40645-015-0056-3.

Amit, H. & Christensen, U.R., 2008. Accounting for magnetic diffusion in core flow inversions from geomagnetic secular variation, *Geophys. J. Int.,* **175,** 913–924.

Amit, H., Deschamps, F. & Choblet, G., 2015b. Numerical dynamos with outer boundary heat flux inferred from probabilistic tomography-consequences for latitudinal distribution of magnetic flux, *Geophys. J. Int.,* **203,** 840–855.

Amit, H. & Olson, P., 2004. Helical core flow from geomagnetic secular variation, *Phys. Earth planet. Inter.,* **147,** 1–25.

Amit, H. & Olson, P., 2006. Time-average and time-dependent parts of core flow, *Phys. Earth planet. Inter.,* **155,** 120–139.

Amit, H. & Olson, P., 2015. Lower mantle superplume growth excites geomagnetic reversals, *Earth planet. Sci. Lett.,* **414,** 68–76.

Amit, H., Olson, P. & Christensen, U.R., 2007. Tests of core flow imaging methods with numerical dynamos, *Geophys. J. Int.,* **168,** 27–39.

Aubert, J., 2015. Geomagnetic forecasts driven by thermal wind dynamics in the Earth's core, *Geophys. J. Int,* **203,** 1738–1751.

Aubert, J., Amit, H. & Hulot, G., 2007. Detecting thermal boundary control in surface flows from numerical dynamos, *Phys. Earth planet. Inter.,* **160,** 143–156.

Aubert, J., Amit, H., Hulot, G. & Olson, P., 2008. Thermo-chemical wind flows couple Earth's inner core growth to mantle heterogeneity, *Nature,* **454,** 758–761.

Aubert, J., Finlay, C.C. & Fournier, F., 2013. Bottom-up control of geomagnetic secular variation by the Earth's inner core, *Nature,* **502,** 219–223.

Aubert, J. & Fournier, A., 2011. Inferring internal properties of Earth's core dynamics and their evolution from surface observations and a numerical geodynamo model, *Nonlin. Proc. Geophys.,* **18,** 657–674.

Aubert, J., Gastine, T. & Fournier, A., 2017. Spherical convective dynamos in the rapidly rotating asymptotic regime, *J. Fluid. Mech.,* **813,** 558–593.

Aurnou, J., Andreadis, S., Zhu, L. & Olson, P., 2003. Experiments on convection in Earth's core tangent cylinder, *Earth planet. Sci. Lett.,* **212,** 119–134.

Barrois, O., Gillet, N. & Aubert, J., 2017. Contributions to the geomagnetic secular variation from a reanalysis of core surface dynamics, *Geophys. J. Int.,* **211**(1), 50–68.

Bloxham, J., 1989. Simple models of fluid flow at the core surface derived from geomagnetic field models, *Geophys. J. Int.,* **99,** 173–182.

Brown, M., Korte, M., Holme, R., Wardinski, I. & Gunnarson, S., 2018. Earth's magnetic field is (probably) not reversing, *Proc. Natl. Acad. Sci.,* **115**(20), 5111–5116.

Brown, M.C., Donadini, F., Korte, M., Nilsson, A., Korhonen, K., Lodge, A., Lengyel, S.N. & Constable, C.G., 2015a. GEOMAGIA50.v3: 1. General structure and modifications to the archeological and volcanic database, *Earth Planets Space,* **67,** 83.

Brown, M.C. *et al.*, 2015b. GEOMAGIA50.v3: 2. A new paleomagnetic database for lake and marine sediments, *Earth Planets Space,* **67,** 70.

Christensen, U.R. & Aubert, J., 2006. Scaling properties of convection-driven dynamos in rotating spherical shells and application to planetary magnetic fields, *Geophys. J. Int.,* **166,** 97–114.

Constable, C., 2007. Centennial- to millennial-scale geomagnetic field variations, in *Treatise on Geophysics,* Vol. **5,** 337–372, Elsevier Sci.

Constable, C.G., Korte, M. & Panovska, S., 2016. Persistent high paleosecular variation activity in Southern Hemisphere for at least 10 000 years, *Earth planet. Sci. Lett.,* **453,** 78–86.

Davies, C.J., Gubbins, D., Willis, A. & Jimack, P.K., 2008. Time-averaged paleomagnetic field and secular variation: predictions from dynamo solutions based on lower mantle seismic tomography, *Phys. Earth planet. Inter.,* **169,** 194–203.

Donadini, F., Korte, M. & Constable, C.G., 2009. Geomagnetic field for 0-3ka: 1. new data sets for global modeling, *Geochem. Geophys. Geosys.,* **10,** doi:10.1029/2008GC002295.

Finlay, C.C., 2008. Historical variation of the geomagnetic axial dipole, *Phys. Earth planet. Inter.,* **170,** 1–14.

Finlay, C.C., Aubert, J. & Gillet, N., 2016. Gyre-driven decay of the Earth's magnetic dipole, *Nat. Commum.,* **7,** 10422, doi:10.1038/ncomms10422.

Finlay, C.C., Olsen, N. & Tøffner-Clausen, L., 2015. DTU candidate field models for IGRF-12 and the CHAOS-5 geomagnetic field model, *Earth Planets Space,* **67,** 114.

Gillet, N., Jault, D. & Finlay, C., 2015. Planetary gyre, time-dependent eddies, torsional waves, and equatorial jets at the Earth's core surface, *J. geophys. Res.,* **120**(6), 3991–4013.

Gubbins, D., 1987. Mechanism for geomagnetic polarity reversals, *Nature,* **326,** 167–169.

Gubbins, D., 2003. Thermal core-mantle interactions: theory and observations, in *Earth's Core: Dynamics, Structure and Rotation,* AGU Geodynamics Series - American Geophysical Union.

Gubbins, D. & Gibbons, S., 2004. Low Pacific secular vatiation, in *Timescales of the Paleomagnetic Field,* American Geophysical Union.

Gubbins, D. & Roberts, N., 1983. Use of the frozen-flux approximation in the interpretation of archaeomagnetic and paleomagnetic data, *Geophys. J. R. astr. Soc.,* **73,** 675–687.

Gubbins, D., Willis, P.W. & Sreenivasan, B., 2007. Correlation of Earth's magnetic field with lower mantle thermal and seismic structure, *Phys. Earth planet. Inter.,* **162,** 256–260.

Hare, V.J., Tarduno, J.A., Huffman, T., Watkeys, M., Thebe, P.C., Manyanga, M., Bono, R.K. & Cottrell, R.D., 2018. New archeomagnetic directional records from Iron Age southern Africa (ca. 425–1550 CE) and implications for the South Atlantic Anomaly, *Geophys. Res. Lett.,* **45,** 1361–1369.

Hartmann, G.A., Genevey, A., Gallet, Y., Trindade, R.I.F., Etchevarne, C., Le Goff, M. & Afonso, M.C., 2010. Archeointensity in Northeast Brazil over the past five centuries, *Earth planet. Sci. Lett.,* **296,** 340–352.

Hartmann, G.A., Genevey, A., Gallet, Y., Trindade, R.I.F., Le Goff, M., Najjar, R., Etchevarne, C. & Afonso, M.C., 2011. New historical archeointensity data from Brazil: Evidence for a large regional non-dipole field contribution over the past few centuries, *Earth planet. Sci. Lett.,* **306,** 66–76.

Hartmann, G.A. & Pacca, I., 2009. Time evolution of the south atlantic magnetic anomaly, *An. Acad. Bras. Cien.,* **81,** 243–255.

Hellio, G. & Gillet, N., 2018. Time-correlation-based regression of the geomagnetic field from archeological and sediment records, *Geophys. J. Int.,* **214**(3), 1585–1607.

Holme, R. & Olsen, N., 2006. Core surface flow modelling from high-resolution secular variation, *Geophys. J. Int.,* **166,** 518–528.

Holme, R., Olsen, N. & Bairstow, F.L., 2011. Mapping geomagnetic secular variation at the core-mantle boundary., *Geophys. J. Int.,* **186,** 521–528.

Hulot, G., Eymin, C., Langlais, B., Mandea, M. & Olsen, N., 2002. Small-scale structure of the geodynamo inferred from Oersted and Magsat satellite data, *Nature,* **416,** 620–623.

Jackson, A., 1997. Time-dependency of tangentially geostrophic core surface motions, *Phys. Earth planet. Inter.,* **103,** 293–311.

Jackson, A., Jonkers, A.R.T. & Walker, M.R., 2000. Four centuries of geomagnetic secular variation from historical records, *Phil. Trans. R. Soc. Lond.,* **A358,** 957–990.

Johnson, C.L. & Constable, C.G., 1997. The time-averaged geomagnetic field: global and regional biases for 0–5 ma, *Geophys. J. Int.,* **131,** 643–666.

Korte, M. & Constable, C.G., 2011. Improving geomagnetic field reconstructions for 0-3 ka, *Phys. Earth planet. Inter,* **188**(3–4), 247–259.

Korte, M., Donadini, F. & Constable, C.G., 2009. The geomagnetic field for 0-3ka: 2. A new series of time-varying global models, *J. geophys. Res.,* Q06008, doi:10.1029/2008GC002297.

Kutzner, C. & Christensen, U.R., 2002. From stable dipolar towards reversing numerical dynamos, *Phys. Earth planet. Inter.,* **131,** 29–45.

Landeau, M. & Aubert, J., 2011. Equatorially antisymmetric convection inducing a hemispherical magnetic field in rotating spheres and implications for the past Martian dynamo, *Phys. Earth planet. Inter.,* **185,** 61–73.

Lekic, V., Cottaar, S., Dziewonski, A. & Romanowicz, B., 2012. Cluster analysis of global lower mantle tomography: a new class of structure and implications for chemical heterogeneity, *Earth planet. Sci. Lett.,* **357,** 68–77.

Licht, A., Hulot, G., Gallet, Y. & Thebault, E., 2013. Ensembles of low degree archeomagnetic field models for the past three millennia, *Phys. Earth planet. Inter.,* **224,** 38–67.

Masters, G., Laske, G., Bolton, H. & Dziewonski, A., 2000. The relative behavior of shear velocity, bulk sound velocity, and compressional velocity in the mantle: Implications for chemical and thermal structure, in *Earth's Deep Interior: Mineral Physics and Tomography From the Atomic to the Global Scale,* Vol. **117,** AGU monograph.

Metman, M.C., Livermore, P.W. & Mound, J.E., 2018. The reversed and normal flux contributions to axial dipole decay for 1880–2015, *Phys. Earth planet. Inter.,* **276,** 106–117.

Mosca, I., Cobden, L., Deuss, A., Ritsema, J.J. &T., 2012. Seismic and mineralogical structures of the lower mantle from probabilistic tomography, *J. geophys. Res.,* **117,** B06304.

Nilsson, A., Holme, R., Korte, M., Suttie, N. & Hill, M., 2014. Reconstructing Holocene geomagnetic field variation: new methods, models and implications, *Geophys. J. Int.,* **198,** 229–248.

Olson, P. & Amit, H., 2006. Changes in earth's dipole, *Naturwissenschaften,* **93,** 519–542.

Olson, P. & Christensen, U.R., 2002. The time averaged magnetic field in numerical dynamos with nonuniform boundary heat flow, *Geophys. J. Int.,* **151,** 809–823.

Olson, P., Christensen, U.R. & Glatzmaier, G.A., 1999. Numerical modeling of the geodynamo: mechanisms of field generation and equilibration, *J. geophys. Res.,* **104,** 10383–110404.

Olson, P., Landeau, M. & Reynolds, E., 2017. Dynamo tests for stratification below the core-mantle boundary, *Phys. Earth planet. Inter.,* **271,** 1–18.

Olson, P., Sumita, I. & Aurnou, J., 2002. Diffusive magnetic images of upwelling patterns in the core, *J. geophys. Res.,* **107,** doi:10.1029/2001jb000384.

Panovska, S. & Constable, C.G., 2017. An activity index for geomagnetic paleosecular variation, excursions, and reversals, *Geochem. Geophys. Geosyst.,* **18,** 1366–1375.

Peña, D., Amit, H. & Pinheiro, K.J., 2016. Magnetic field stretching at the top of the shell of numerical dynamos, *Earth Planets Space,* **38,** 48.

Poletti, W., Trindade, R.I.F., Hartmann, G.A., Damiani, N. & Rech, R.M., 2016. Archeomagnetism of Jesuit Missions in South Brazil (1657–1706 AD) and assessment of the South American database, *Earth planet. Sci. Lett.,* **445,** 63–47.

Sanchez, S., Fournier, A., Aubert, J., Cosme, E. & Gallet, Y., 2016. Modelling the archaeomagnetic field under spatial constraints from dynamo simulations: a resolution analysis, *Geophys. J. Int.,* **207**(2), 983–1002.

Schaeffer, N., Jault, D., Nataf, H.-C. & Fournier, A., 2017. Turbulent geodynamo simulations: a leap towards Earth's core, *Geophys. J. Int,* **189,** 1–29.

Shah, J. *et al.*, 2016. Paleomagnetic evidence for persistence of recurrence of geomagnetic main field anomalies in the South Atlantic., *Earth planet. Sci. Lett.,* **441,** 113–124.

Sumita, I. & Olson, P., 1999. Laboratory model for convection in Earth's core driven by a thermally heterogeneous mantle, *Science,* **286,** 1547–1549.

Sumita, I. & Olson, P., 2002. Rotating thermal convection experiments in a hemispherical shell with heterogeneous boundary heat flux: Implications for the Earth's core, *J. geophys. Res.,* **107**(B8), 2169.

Takahashi, F., Tsunakawa, H., Matsushima, M., Mochizuki, N. & Honkura, Y., 2008. Effects of thermally heterogeneous structure in the lowermost mantle on the geomagnetic field strength, *Earth planet. Sci. Lett.,* **272**(3–4), 738–746.

Tarduno, J.A., Watkeys, M.K., Huffman, T.N., Cottrell, D.C., Blackman, E.G., Wendt, A., Scribner, A.C. & Wagner, C.L., 2015. Antiquity of the South Atantic Anomaly and evidence for top-down control on the geodynamo, *Nat. Commun.,* **6,** 7865, doi:10.1038/ncomms8865.

Terra-Nova, F., Amit, H., Hartmann, G.A. & Trindade, R.I.F., 2015. The time dependence of reversed archeomagnetic flux patches, *J. geophys. Res.,* **120**(2), 691–704.

Terra-Nova, F., Amit, H., Hartmann, G.A. & Trindade, R.I.F., 2016. Using archaeomagnetic field models to constrain the physics of the core: robustness and preferred locations of reversed flux patches, *Geophys. J. Int.,* **206**(3), 1890–1913.

Terra-Nova, F., Amit, H., Hartmann, G.A., Trindade, R.I.F. & Pinheiro, K.J., 2017. Relating the South Atlantic Anomaly and geomagnetic flux patches, *Phys. Earth planet. Inter.,* **266,** 39–53.

Thébault, E. *et al.*, 2015. International Geomagnetic Reference Field: the twelfth generation., *Earth Planets Space,* **67,** 79, doi:10.1186/s40623–015–0228–9.

Trindade, R. I. F. *et al.*, 2018. Speleothem record of geomagnetic South Atlantic Anomaly recurrence, *Proc Natl Acad Sci USA,* **115,** 13198–13203.

Wicht, J., 2002. Inner-core conductivity in numerical dynamo simulations, *Phys. Earth planet. Inter.,* **132,** 281–302.